

Westward mountain-gap wind jets of the northern Red Sea as seen by QuikSCAT

Viviane V. Menezes^{*}, J. Thomas Farrar, Amy S. Bower

Physical Oceanography Department, Woods Hole Oceanographic Institution 266 Woods Hole Rd, Clark 316B MS#21, Woods Hole, MA, 02540, United States

ARTICLE INFO

Keywords:

QuikSCAT
Air-sea interaction
Wind jets
Mountain gap
Evaporation
Heat loss

ABSTRACT

We analyse ten years of QuikSCAT satellite surface winds to statistically characterize the spatio-temporal variability of the westward mountain-gap wind jets over the northern Red Sea. These wind jets bring relatively cold and dry air from the Arabian Desert, increasing heat loss and evaporation over the region similar to cold-air outbreaks from mid and subpolar latitudes. QuikSCAT captures the spatial structure of the wind jets and agrees well with in situ observations from a heavily instrumented mooring in the northern Red Sea. The local linear correlations between QuikSCAT and in situ winds are 0.96 (speed) and 0.85 (direction). QuikSCAT also reveals that cross-axis winds such as the mountain-gap wind jets are a major component of the regional wind variability. The cross-axis wind pattern appears as the second (or third) mode in the four vector Empirical Orthogonal Function analyses we performed, explaining between 6% to 11% of the wind variance. Westward wind jets are typical in winter, especially in December and January, but with strong interannual variability. Several jets can occur simultaneously and cover a large latitudinal range of the northern Red Sea, which we call large-scale westward events. QuikSCAT recorded 18 large-scale events over ten years, with duration between 3 to 8 days and strengths varying from 3–4 to 9–10 m/s. These events cause large changes in the wind stress curl pattern, imposing a remarkable sequence of positive and negative curl along the Red Sea main axis, which might be a wind forcing mechanism for the oceanic mesoscale circulation.

1. Introduction

For about 10 years, the Seawinds/QuikSCAT satellite mission from NASA (National Aeronautics and Space Administration) provided an unprecedented view of the near-surface vector winds over the global oceans (e.g. Cornillon and Park, 2001; Chelton et al., 2004; Chelton et al., 2006; Ebuchi et al., 2002; Fu and Morrow, 2013; Hoffman and Leidner, 2005; Holbach and Bourassa, 2014; Kelly et al., 2001; O'Neill et al., 2005; O'Neill et al., 2010; Risien and Chelton, 2008). Notably, QuikSCAT captured persistent small-scale features in the wind stress curl and divergence fields in coastal regions where orography influences the near-surface winds such as the mountain-gap wind jets of Tehuantepec, Papagayo and Panama in the Pacific coast of Central America (Brennan and Cobb, 2010; Chelton et al., 2004; Holbach and Bourassa, 2014).

The fact that QuikSCAT captures orographic-associated features motivated us to examine this dataset to understand the largely unknown westward mountain-gap wind jets over the northern Red Sea (Jiang et al., 2009). The Red Sea, an Indian Ocean marginal sea, is surrounded by mountains on both sides of the basin (Fig. 1). These

mountains constrain the prevailing winds to blow approximately along the Red Sea main axis (Fig. 2). But synoptic conditions can sometimes cause the winds to blow across the axis through the mountain-gaps from both sides of the basin.

Besides orography, the large-scale Indian monsoon system and the regional land-sea breeze govern the Red Sea wind variability (e.g., Churchill et al., 2014; Davis et al., 2015; Patzert, 1974; Sofianos and Johns, 2003; Steedman and Ashour, 1976). Sea breeze-like circulation is responsible for the largest part (about 80%) of the moisture transport between the Red Sea and the surrounding dry lands at least in the ERA-Interim dataset (Zolina et al., 2017). QuikSCAT, however, is unable to fully resolve the diurnal cycle associated with the Red Sea breezes because its sampling frequency is at best twice a day at each location (e.g., Gille et al., 2003); hence, this subject falls outside the scope of the present study.

Because of the monsoons, the Red Sea surface winds have a seasonally dependent spatial pattern (Clifford et al., 1997; Johns et al., 1999; Langodan et al., 2017; Patzert, 1974; Sofianos and Johns, 2003). Over the northern Red Sea (north of 20° N), the along-axis winds are predominantly southward all year-round, but in the southern basin they

^{*} Corresponding author.

E-mail address: vmenezes@whoi.edu (V.V. Menezes).

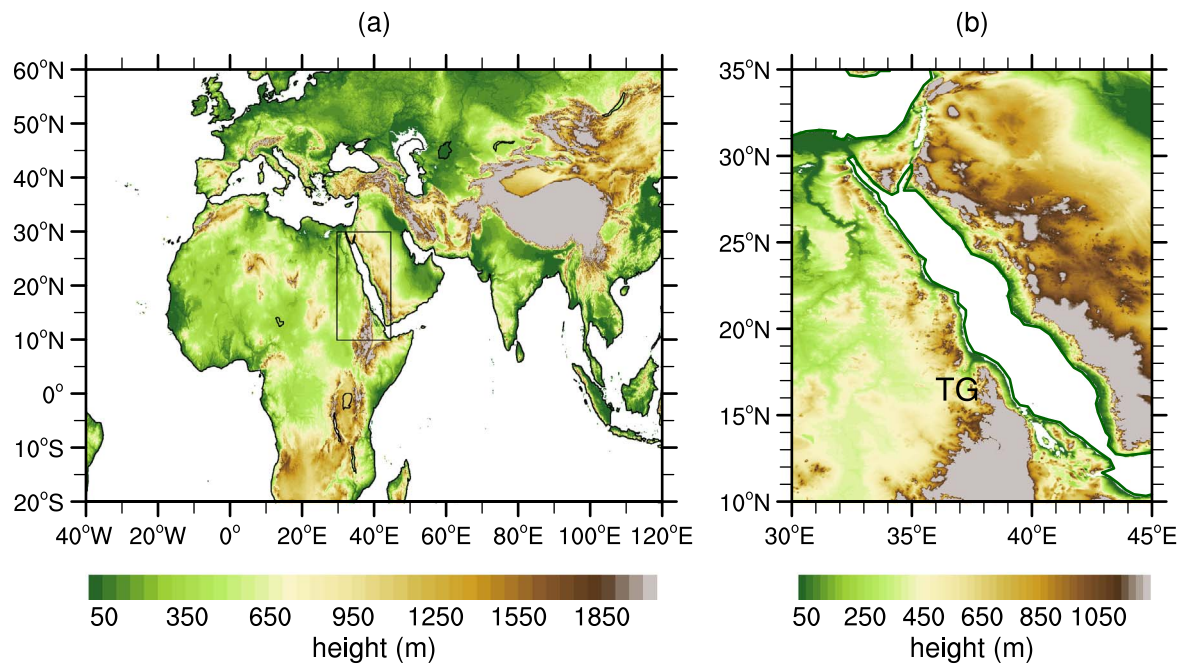


Fig. 1. Land elevation from the ETOPO2 Global Relief data (see Section 2.3 for a description about this dataset): (a) Large-scale view, including Africa, Europa and Asia. Black rectangle highlights the Red Sea (b) Land elevation surrounding the Red Sea. The colorbars in (a) and (b) have different ranges. TG stands for Tokar Gap. (For interpretation of the references to color in this figure legend, the reader is referred to the web version of this article.)

reverse seasonally due to the monsoonal regime (Fig. 2). Hence, during the summer monsoon (May–September), the climatological winds blow southward over the entire Red Sea (Fig. 2 e–i). In the winter monsoon (October–April), the winds in the northern and southern basins blow in opposite directions, forming a climatological convergence zone near 19° N (Fig. 2 l–m). Pedgley (1966a) defined the cloudy area with calm or light winds where the two opposite-blowing air-streams meet as the Red Sea Convergence Zone (RSCZ) (Fig. 3c). This definition has been used in several works since then (e.g., Langodan et al., 2015; Patzert, 1974; Ralston et al., 2013; Viswanadhapalli et al., 2017; Zolina et al., 2017).

The pioneer studies of Pedgley (1966a,b) were motivated by the fact that the RSCZ controls the northward migration of the Desert Locust swarms, a plague that periodically hits the bordering countries of the Red Sea as already described in the Old Testament of the Bible. Based on along-axis wind data from February 1964, Pedgley (1966a,b) inferred that the RSCZ migrates in a north-south direction, with its northward position reaching Jeddah at 21.28° N (Fig. 3a). The meridional migration of the RSCZ was later confirmed by Patzert (1974). In the QuikSCAT climatological winds, the RSCZ is better defined in November and December and located at about 19° N. Under the RSCZ, the northward and southward winds bend westward towards the Tokar Gap on the Sudanese coast (18° N–19° N, TG in Fig. 1b). The narrow band of westward winds between 18° N–19° N associated with the RSCZ seen in QuikSCAT also appear in model simulations and reanalysis products (e.g., Jiang et al., 2009; Viswanadhapalli et al., 2017). Johns et al. (1999) describe the RSCZ as the limit between the monsoon-dominated atmosphere in the south and the continental atmosphere in the north.

Despite the surface winds being predominantly along the main axis, several works describe the winds occasionally blowing in a cross-axis direction through mountain gaps on both sides of the Red Sea (e.g., Bower and Farrar, 2015; Clifford et al., 1997; Davis et al., 2015; Jiang et al., 2009; Zhai and Bower, 2013). These mountain-gap cross-axis winds have no clear signature in the climatological monthly means. In the central Red Sea, cross-axis winds occur in summer (hereafter boreal seasons), with winds blowing eastward through the Tokar Gap (Davis et al., 2015; Jiang et al., 2009; Zhai and Bower, 2013). Zhai and Bower

(2013) found strong evidence that the Tokar Gap wind jet leads to the formation of oceanic dipole eddies between 18° N–20° N, similar to the effects of the Tehuantepec, Panama and Papagayo wind jets (e.g., McCreary et al., 1989; Chelton et al., 2000; Kessler, 2006). Numerical simulations using ROMS (Regional Ocean Modelling Systems) by Farley Nicholls et al. (2015) corroborate these findings.

Much less is understood about the cross-axis winds blowing through the mountain gaps in the northern Red Sea. Differently from the Tokar Gap wind jet, the northern Red Sea jets are predominantly westward, from Saudi Arabia to Africa, and occur in winter (Jiang et al., 2009; Bower and Farrar, 2015). These wintertime events are distinct from the narrow RSCZ-associated westward winds because the mountain-gap winds bring relatively cold dry air and dust from the desert and are formed by multiple jets extending over a large latitudinal range (Bower and Farrar, 2015; Jiang et al., 2009; Kalenderski et al., 2013). However, most of the knowledge about the westward wind jets is based on short-time numerical simulations using the Weather Research and Forecasting (WRF) model (e.g. Jiang et al., 2009; Kalenderski et al., 2013) and no statistics (e.g., frequency, duration) about them existed until the present study. The simulations are for periods of 60 days or less between December 2008 and January 2009, and focus on a single event on 14–15 January 2009. To the best of our knowledge no comprehensive study about the westward mountain-gap wind-jet events based on satellite observations has been realized to date.

During westward wind-jet events, relatively strong winds (up to 15 m/s) and cold dry air cause episodes of large oceanic heat loss (-700 to -900 W/m²) and high evaporation (> 5 m/yr) in the northern Red Sea (Jiang et al., 2009; Bower and Farrar, 2015). Hence, the westward events resemble the severe cold-air outbreaks that occur in mid and subpolar latitudes such as over the Gulf Stream region (oceanic heat loss of about 1000 W/m²) (e.g., Marshall et al., 2009), the Japan/East Sea (> 400 W/m²) (e.g., Dorman et al., 2006) and the borawinds in the Adriatic Sea (700 W/m²) (e.g., Lee et al., 2005, Poulain and Cushman-Roisin, 2001)

Because the westward events cause strong heat loss and evaporation, they may trigger surface water mass transformation that can lead to the formation of Red Sea Overflow Water (Bower and Farrar, 2015;

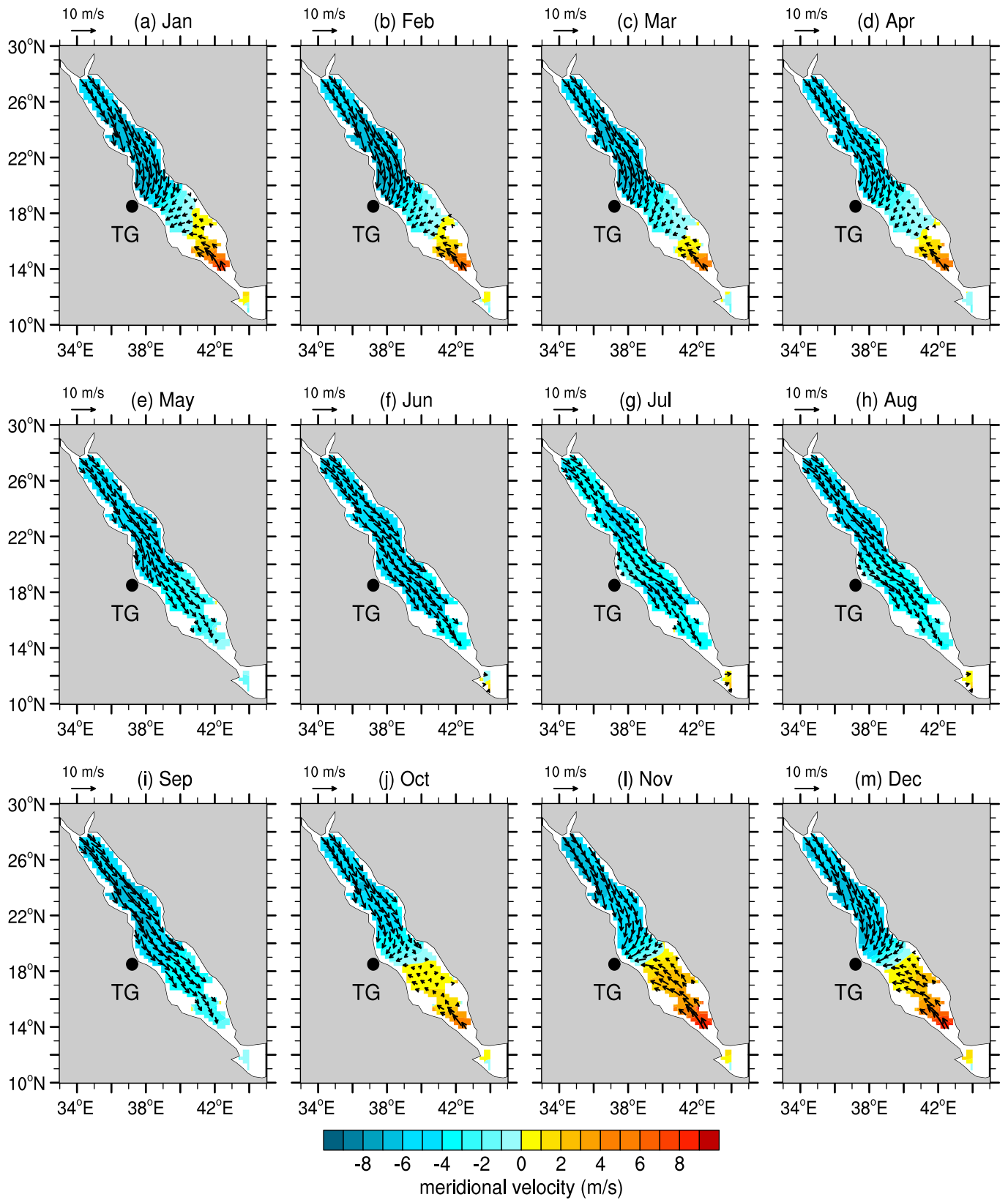


Fig. 2. Climatological monthly mean wind fields from QuikSCAT satellite scatterometer (1999–2009). Color indicates the meridional wind velocity using the colorbar at bottom of the page. Black dot shows the position of the Tokar Gap (TG) on the Sudanese coast. For display purposes, vectors are shown with a coarsened resolution of 0.02 (normalized device coordinates) from the NCAR Command Language (NCL, 2017), which is approximately 1.3° (geographic coordinates). (For interpretation of the references to color in this figure legend, the reader is referred to the web version of this article.)

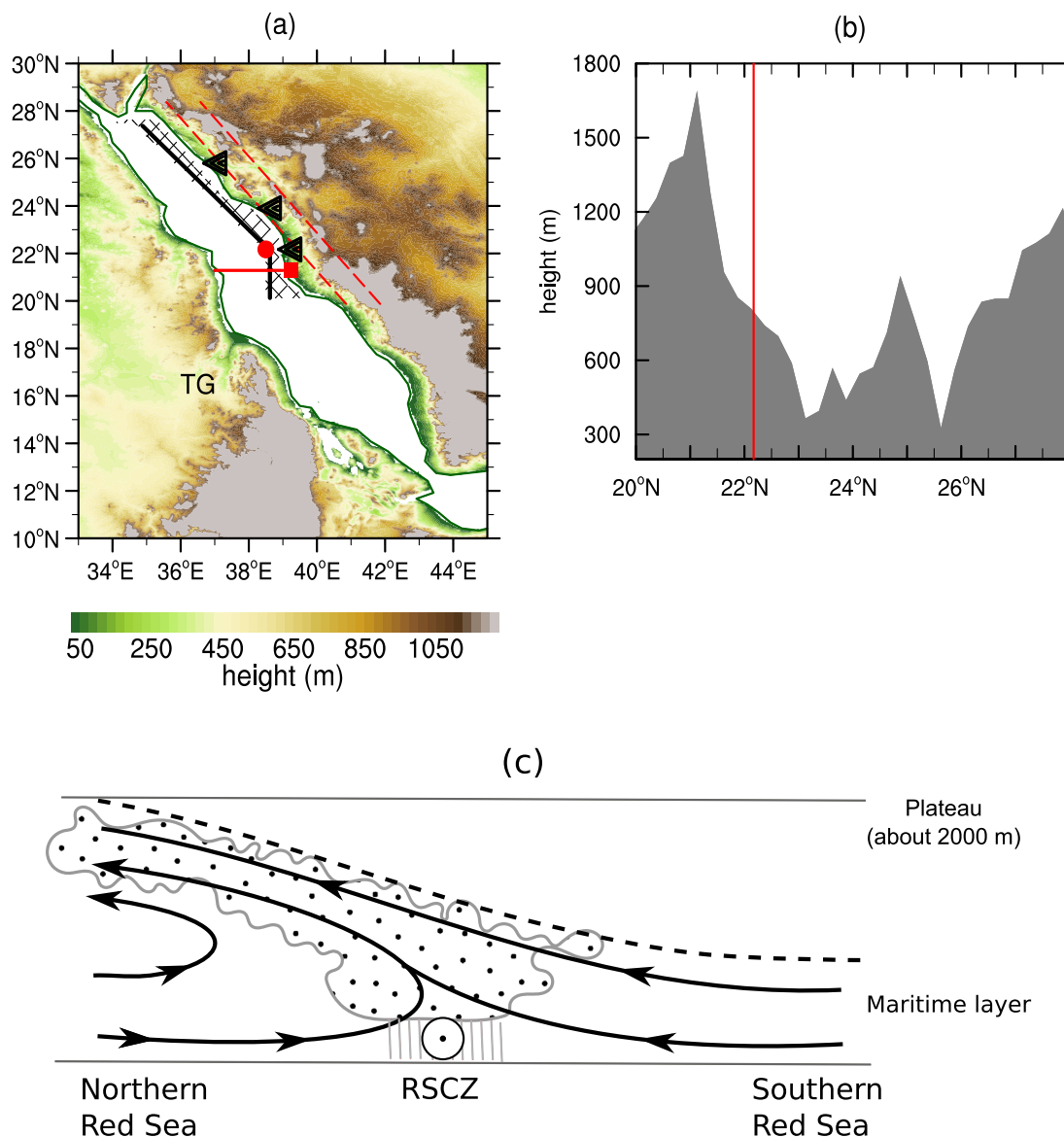


Fig. 3. (a) Relief along the Red Sea based on the global ETOPO-2 data. The black line is the reference line and the dashed area indicates the eastern boundary region. The reference line extends for 7.25° in latitude from 20.125° N to 27.375° N. The red dot shows the WHOI/KAUST mooring position, the red square the position of Jeddah in Saudi Arabia and the red line indicate the Jeddah latitude across the Red Sea. The left pointed black triangles indicate the position of the three main wind jets identified in the WRF simulation (see Fig. 5). TG stands for Tokar Gap. (b) Mean elevation (gray shading) of the Hijaz-Asir Mountains averaged in the region between the dashed red lines over Saudi Arabia in (a). The vertical line in (b) marks the mooring position. (c) Schematic diagram of the RSCZ adapted from Pedgley (1966b). (For interpretation of the references to color in this figure legend, the reader is referred to the web version of this article.)

Papadopoulos et al., 2013). This water mass is one of the most important global sources of salt for the intermediate layer of the oceans; thus, air-sea interactions in the interior of the Red Sea may have large-scale effects (e.g., Beal et al., 2000; Han and McCreary, 2001). Westward events may increase eddy activity in the northern Red Sea as suggested by the earlier numerical simulations of Clifford et al. (1997) and by the studies of Zhai and Bower (2013) and Farley Nicholls et al. (2015), and may also alter the Red Sea wave climate (Ralston et al., 2013; Langodan et al., 2014). Moreover, results from Kalenderski et al. (2013) indicate that the dust associated with the westward winds may increase nutrients in surface waters and reduce the solar radiation reaching the sea surface. However, the exact role played by westward winds for the Red Sea circulation and ecosystem are speculative at this point because even basic statistics about these wind events are unknown.

In the present work, we analyse 10-years of QuikSCAT satellite scatterometer winds to statistically characterize the spatio-temporal

variability of the surface westward mountain-gap wind jet events over the northern Red Sea. The study is complemented with in situ wind measurements collected at 22.17° N– 38.5° E between October 2008 and December 2010 (Bower and Farrar, 2015).

This paper is organized as follows: Sections 2 and 3 describe the datasets and the methods, respectively; Section 4.1 presents an evaluation of the QuikSCAT winds against in situ measurements and the WRF-simulated wind jets from Jiang et al. (2009); Section 4.2 gives the statistics of the westward mountain-gap wind jets; Section 4.3 focuses on the large-scale events and Section 4.4 on vector EOF (Empirical Orthogonal Function) analyses of the wind fields; Section 5 provides the summary and discussion.

2. Data

2.1. QuikSCAT winds

The primary wind data analysed in the present study are the ocean surface vector winds collected by QuikSCAT between July 1999 and November 2009, when the satellite experienced a mechanical failure. QuikSCAT is an active microwave radar operating at Ku band (13.4 GHz) in a sun-synchronous, near polar orbit at 803 km of altitude, with a swath width of 1800 km. Its repeat cycle is about 4 days (57 orbits formed by ascending/descending passes) with approximately 90% of Earth covered daily (Ebuchi et al., 2002; Hoffman and Leidner, 2005; Risien and Chelton, 2008). QuikSCAT measures winds between 3–30 m/s with accuracy of 2 m/s and 20° in direction over ice-free oceans, approximately twice a day at each location, with a nominal spatial resolution of 25 km. Ascending and descending passes occur around 6:00 and 18:00 local equatorial crossing time, respectively. QuikSCAT accuracy is known to degrade at very high and very low wind speeds and at moderate to heavy rainfall (e.g. Chelton et al., 2006; Hoffman and Leidner, 2005; Ricciardulli and Wentz, 2015; Weissman et al., 2002). The QuikSCAT vector winds are retrieved within 15–30 km off coastlines, and adjusted to be the equivalent to winds at 10 m height (above the sea surface) under neutral stratification conditions. In the Red Sea, ascending (north-bound) and descending (south-bound) passes are between 0300–0400 and 1500–1600 UTC, respectively.

Satellite scatterometers actually retrieve winds relative to the sea surface currents and not in relation to a motionless referential, therefore scatterometers winds tend to be stronger than anemometer measurements when the winds oppose the currents and vice-versa (Cornillon and Park, 2001; Kelly et al., 2001).

The QuikSCAT datasets used in the present work belong to the level-3, gridded product series (0.25° × 0.25°) version 4 produced by Remote Sensing Systems (RSS). In this version, QuikSCAT data have been processed using the 2011 Ku-band Geophysical Model Function (GMF) that improves wind direction retrievals at very low (< 5 m/s) and high wind speeds (> 15 m/s) (Ricciardulli et al., 2011; Ricciardulli and Wentz, 2015). The RSS rain detection algorithm is based on data from four passive microwave radiometers from TMI (Tropical Rainfall Measuring Mission) and SSM/I (Special Sensor Microwave Imager, onboard of F13, F14 and F15 satellites from the Defense Meteorological Satellite Program). Here, only pixels that are not contaminated by rain are used, although precipitation is extremely low over the Red Sea (Tragou et al., 1999). We use both the daily product containing ascending/descending pass swath data and the 3-day moving average product described below.

Westward wind jet statistics are computed from the RSS 3-day moving average product because it offers better spatial coverage over the northern Red Sea (e.g. Fig. 4) and smooths the strong diurnal cycle associated with the land-sea breeze (Churchill et al., 2014; Davis et al., 2015). For comparison with in situ observations and model snapshots, the ascending/descending version is used. Dates in the 3-day moving average product refer to the last day of the temporal window.

In the RSS 3-day moving average product, wind speeds are scalar averaged and directions are vector averaged (Ricciardulli et al., 2011). Averages were only calculated if there were at least two valid measurements during the 3-day period. The data span from 20 July 1999 to 19 November 2009 at daily time steps. In the Red Sea, there are very few temporal gaps in the 3-day moving average dataset (0.32%), which are generally due to periods when QuikSCAT was turned off. We filled in these gaps by linear interpolation in time. For that, the speed and direction fields were projected to zonal (u) and meridional (v) wind components, and u and v fields were temporally interpolated.

Wind stress fields (τ^x, τ^y) and curl were derived from the ascending and descending pass data. This dataset consists of swath passes individually projected into a 0.25° bin resolution. We estimate τ^x and τ^y

using the bulk formula:

$$\tau^x(t) = \rho_a c_d(t) W(t) u(t) \quad (1)$$

$$\tau^y(t) = \rho_a c_d W(t) v(t) \quad (2)$$

where ρ_a is the air density (constant and equal to 1.22 kg m⁻³), u and v are the zonal and meridional velocity fields in m/s, respectively, W is the wind speed given by $\sqrt{u^2 + v^2}$ and c_d is the drag coefficient from Large et al. (1994) $((2.70/W + 0.142 + 0.0764W) \times 10^{-3})$. This is the same drag coefficient used by Risien and Chelton (2008) to compute the QuikSCAT Scatterometer Climatology of Ocean Winds (SCOW). Discussion about the impact of different drag coefficient formulations can be found in Appendix B of Risien and Chelton (2008) and also in Brodeau et al. (2017). According to Risien and Chelton (2008), COARE 3.0 (Coupled Ocean Atmosphere Response Experiment) scheme (Fairall et al., 2003) result in stronger wind stress fields (about 15%) than the ones estimated using Large et al. (1994).

Besides the drag coefficient, another source of uncertainty in our wind stress estimation is the constant air density as discussed by Brodeau et al. (2017). In the Red Sea, this uncertainty is 3–5 % according to Fig. 3 of Brodeau et al. (2017). For each ascending and descending field, we estimate the wind stress curl (vertical component) as $\text{curl} = \partial\tau^y/\partial x - \partial\tau^x/\partial y$ using finite central differences. The ascending/descending wind stress and curl fields are then used to compute the 3-day moving averages.

2.2. WHOI/KAUST mooring

In situ winds from a surface buoy moored at 693 m depth at 22° 10' N and 38° 30' E are also analysed (Fig. 3a, red dot). This mooring was deployed by the Woods Hole Oceanographic Institution (WHOI) in collaboration with the King Abdullah University of Science and Technology (KAUST) to study air-sea interaction in the Red Sea (Farrar et al., 2009). There were two, one year mooring deployments covering the 25 month period from 11 October 2008 14:30 to 17 December 2010 04:30 UTC. The mooring was located west of a gap between the Hijaz and Asir Mountains (Fig. 3a–b), the coastal escarpment that extends through the west coast of the Arabian Peninsula, and within one of the westward wind jets described by Jiang et al. (2009) (Fig. 5). Therefore, the mooring is in a good location for evaluating the westward mountain-gap winds.

The following parameters were measured at the buoy: temperature, salinity and ocean currents, wind velocity and direction, air temperature, humidity, barometric pressure, incoming shortwave (incident sunlight) and longwave (infrared) radiation, precipitation, and surface waves. Most parameters were measured once per minute (Farrar et al., 2009). To be comparable to the QuikSCAT winds, the hourly wind measurements were converted to winds at 10 m height (relative to the sea surface) under neutral atmospheric stratification conditions. This conversion was done using the air-sea flux data measured at the mooring and the COARE 3.0 bulk flux algorithm (Fairall et al., 2003).

The WHOI/KAUST wind time series spans 25 months and is almost complete with only 0.3% of missing data, due to the replacement time of the mooring after the first year of operation. The small gaps were filled by linear interpolation.

2.3. Auxiliary datasets: ETOPO2 and WRF outputs

The 2-Minute Gridded Global Relief Data, best known as ETOPO-2, is used to identify topographic features. ETOPO-2 version 2, published in 2006, is available through the National Geophysical Data Center (NGDC, 2006). It contains relief data for both ocean and land areas. Ocean bathymetry is from the dataset produced by Smith and Sandwell (1997), which is mostly based on satellite altimetry. Land topography is compiled from several sources that include the Global Land One-kilometer Base Elevation (GLOBE) database, the International Bathymetric

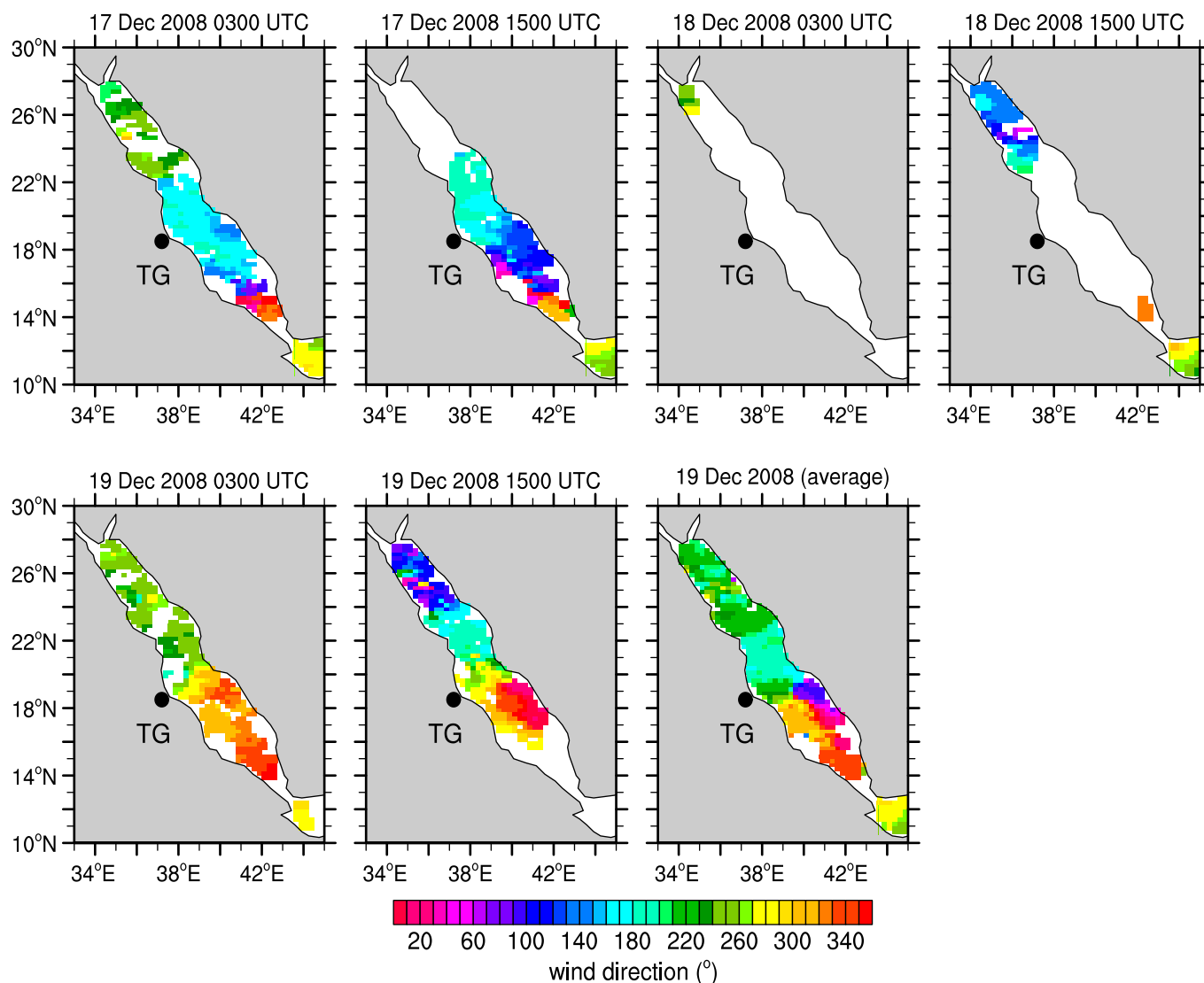


Fig. 4. Wind direction (oceanographic convention) from six QuikSCAT passes from 17 December 2008 to 19 December 2008, which were used to compute the 3-day average shown in the last map (19 December 2008). In the northern Red Sea, the mean direction is westward (215°–280°, greenish). (For interpretation of the references to color in this figure legend, the reader is referred to the web version of this article.)

Chart of the Arctic Ocean, Coastal Relief Model and Great Lakes Bathymetric Data from the National Centers for Environmental Information and digitalized data from the Caspian Environment Programme.

We also compare the QuikSCAT spatial pattern on 15 January 2009 with the WRF outputs from Jiang et al. (2009). These simulated wind fields were kindly supplied by Houshuo Jiang from WHOI and have horizontal grid resolution of 10 km at hourly time steps. This WRF simulation is a downscale of the coarse resolution NCEP (National Centers for Environmental Prediction) Global Final Analysis to the Red Sea domain (see Jiang et al., 2009, for a complete description).

3. Methods

3.1. Evaluation of the QuikSCAT winds

For the comparison with in situ observations, we use the daily ascending/descending QuikSCAT data from the closest grid point (13.57 km) to the WHOI/KAUST mooring. This QuikSCAT dataset consists of winds collected approximately twice a day (0300–0400 and 1500–1600 UTC). No temporal interpolation is performed. From the

mooring data, we select the measurements closest to the QuikSCAT observations in time (< 1 h). We refer to these data pairs (QuikSCAT, mooring) as collocated observations. Since we have concomitant in situ near-surface currents measured at the mooring, the in situ winds are corrected for the surface currents to be consistent with the satellite data. The overlapping period between in situ winds, currents and QuikSCAT data spans from 13 October 2008 to 1 November 2009. In this period, there are 515 collocated observations. Both satellite and in situ winds contain errors and uncertainties, and the collocations between them are not exact (e.g., Bourassa et al., 2003; Hoffman and Leidner, 2005; Stoffelen, 1988). For example, variability in scales smaller than the satellite spatial resolution will not be captured by QuikSCAT but can be measured at the mooring. Unfortunately, this issue is hard to assess because our in situ winds are from one point inside the satellite footprint. Temporal sampling and averaging can also contribute to mismatch satellite and in situ winds. Because the original in situ wind time series has 1 min resolution, we can estimate the effect of the temporal-interval averaging on the collocation. For that, we compare the same QuikSCAT observations with in situ winds averaged over different intervals: from 2 min to 23 h. In this case, no correction for surface currents is applied because our ocean current velocities do

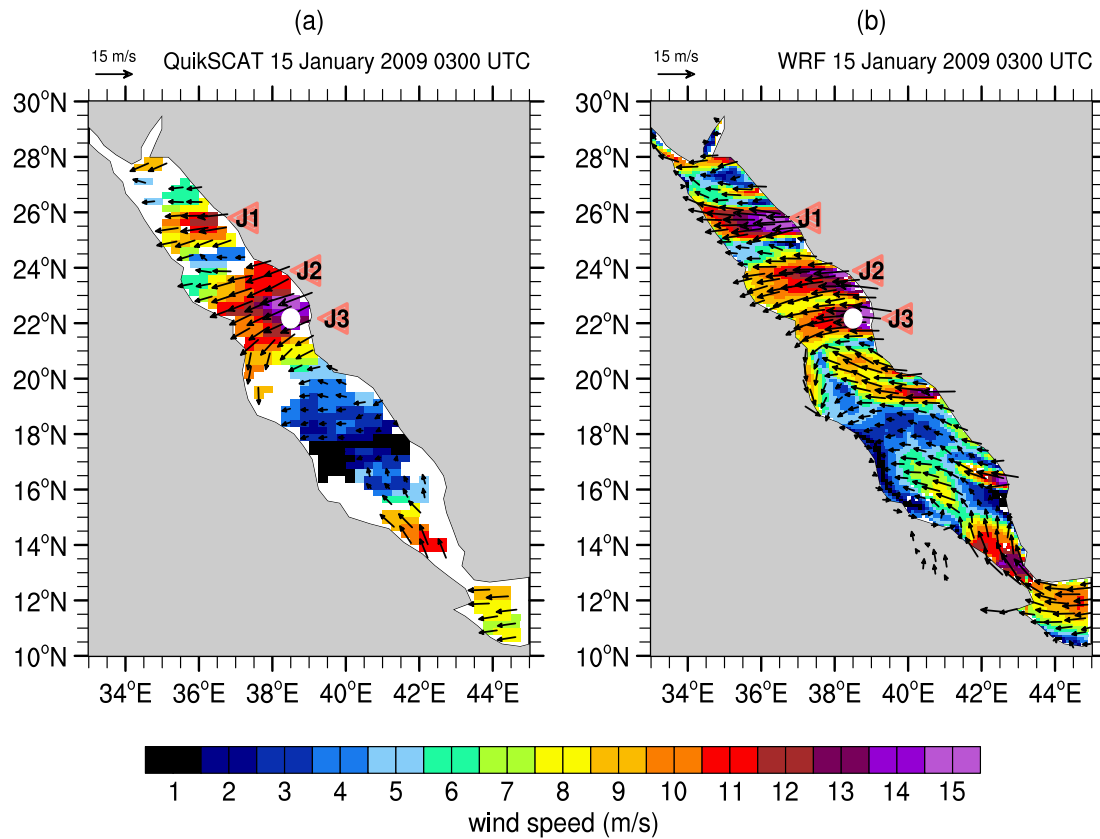


Fig. 5. Westward wind jets on 15 January 2009 0300 UTC as seen by the QuikSCAT morning pass (a) and WRF simulation by Jiang et al. (2009) (b). Color indicates the wind speeds using the colorbar at bottom of the page. White dot shows the WHOI/KAUST mooring position. Left pointed triangles indicate the position of the three main wind jets identified in the WRF simulation (J1, J2 and J3). For display purposes, vectors in (a) and (b) are shown with a coarsened resolution (approximately 0.57°). (For interpretation of the references to color in this figure legend, the reader is referred to the web version of this article.)

Table 1

Comparison between winds from QuikSCAT ascending/descending passes and the hourly-average measurements at the WHOI/KAUST mooring (22.17° N; 38.5° E) for the period 13 October 2008–11 November 2009. In situ winds have been corrected for the surface currents *a priori*. The upper block shows the mean and the standard deviation (σ) for wind speed (SPD) and wind direction (DIR) of each dataset. The middle block shows the same information but for zonal (u) and meridional (v) wind components. The lower block shows the mean difference ($\mu(\Delta)$) between QuikSCAT and in situ observations, the root mean square of the difference ($rmsd$ (Δ)) and the linear correlation coefficients (R), which are significantly different from zero at 95% confidence. Values between brackets are the respective statistics for in situ wind speeds above 3 m/s.

	μ_{SPD} (m/s)	σ_{SPD} (m/s)	μ_{DIR} (°)	σ_{DIR} (°)
QuikSCAT	6.13 [6.89]	2.84 [2.45]	155.96 [154.02]	43.18 [34.72]
Mooring	6.06 [6.86]	2.79 [2.32]	145.43 [144.35]	39.20 [32.73]
	μ_u (m/s)	σ_u (m/s)	μ_v (m/s)	σ_v (m/s)
QuikSCAT	2.11 [2.51]	2.87 [2.88]	-4.55 [-5.28]	3.51 [3.31]
Mooring	2.91 [3.41]	3.04 [3.02]	-4.17 [-4.82]	3.07 [2.90]
	$\mu(\Delta)$	$rmsd$ (Δ)	R	
Speed	0.08 [0.03]	0.75 [0.72]	0.96 [0.96]	
Direction	15.31 [11.82]	25.58 [17.37]	0.72 [0.85]	
u	-0.80 [-0.89]	1.39 [1.38]	0.89 [0.89]	
v	-0.39 [-0.46]	1.66 [1.70]	0.88 [0.86]	

not have the same fine temporal resolution.

To evaluate the QuikSCAT data, descriptive statistics (e.g., mean, standard deviation, linear correlation coefficient, root-mean-square of the difference, statistical distribution) are calculated separately for wind speed, direction, u and v . For direction, we used circular statistics (Fisher, 1996; Zar, 2010). For example, the circular mean of a set of angles ($a_i, i = 1..m$) is defined as $\bar{a} = \arctan(y/x)$, where

$x = \sum_{i=1}^m \cos(a_i)$ and $y = \sum_{i=1}^m \sin(a_i)$ (Zar, 2010). The respective standard deviation is given by $\sigma_a = \sqrt{-2 \ln(R/m)}$, where $R = \sqrt{x^2 + y^2}$. More details about circular statistics can be found in Berens (2009), Fisher (1996) and Zar (2010).

3.2. Statistics of cross-axis westward winds

The present work aims to statistically characterize the westward wind events that come from the desert through the mountain gaps along the Saudi Arabian coast such as the event on 15 January 2009 (Fig. 5). To this end, the QuikSCAT grid points eastward of a slanted line parallel to the Saudi Arabian coast are selected (Fig. 3a, dashed area). Hereafter, we refer to this line as the reference line, which is located about 100 km offshore of the Saudi Arabian coast and passes over the WHOI/KAUST mooring position (Fig. 3a, red dot). Notice that the QuikSCAT winds are not measured over land and are only defined 15–30 km off the coastline. If the winds are westward in the eastern boundary region, they are very likely to come from land, except in the southern limit of our study area (20° N) where westward winds may include the RSCZ-associate westward winds when this zone exists (Fig. 2 j–m).

We define a “westward” wind event as the occurrence of persistent winds in the direction range of 215° to 280°. All wind directions in the present work are given in the oceanographic convention, i.e., the direction to where the wind blows. Holbach and Bourassa (2014) also adopt a criterion based on wind direction to define the mountain-gap wind jets of Papagayo and Tehuantepec. Because the northern Red Sea is slanted in relation to the North-South coordinate axis (about 38°–45° to the west of the geographic North), its cross axis is not aligned with the geographic East-West axis. A cross-axis wind with a westward

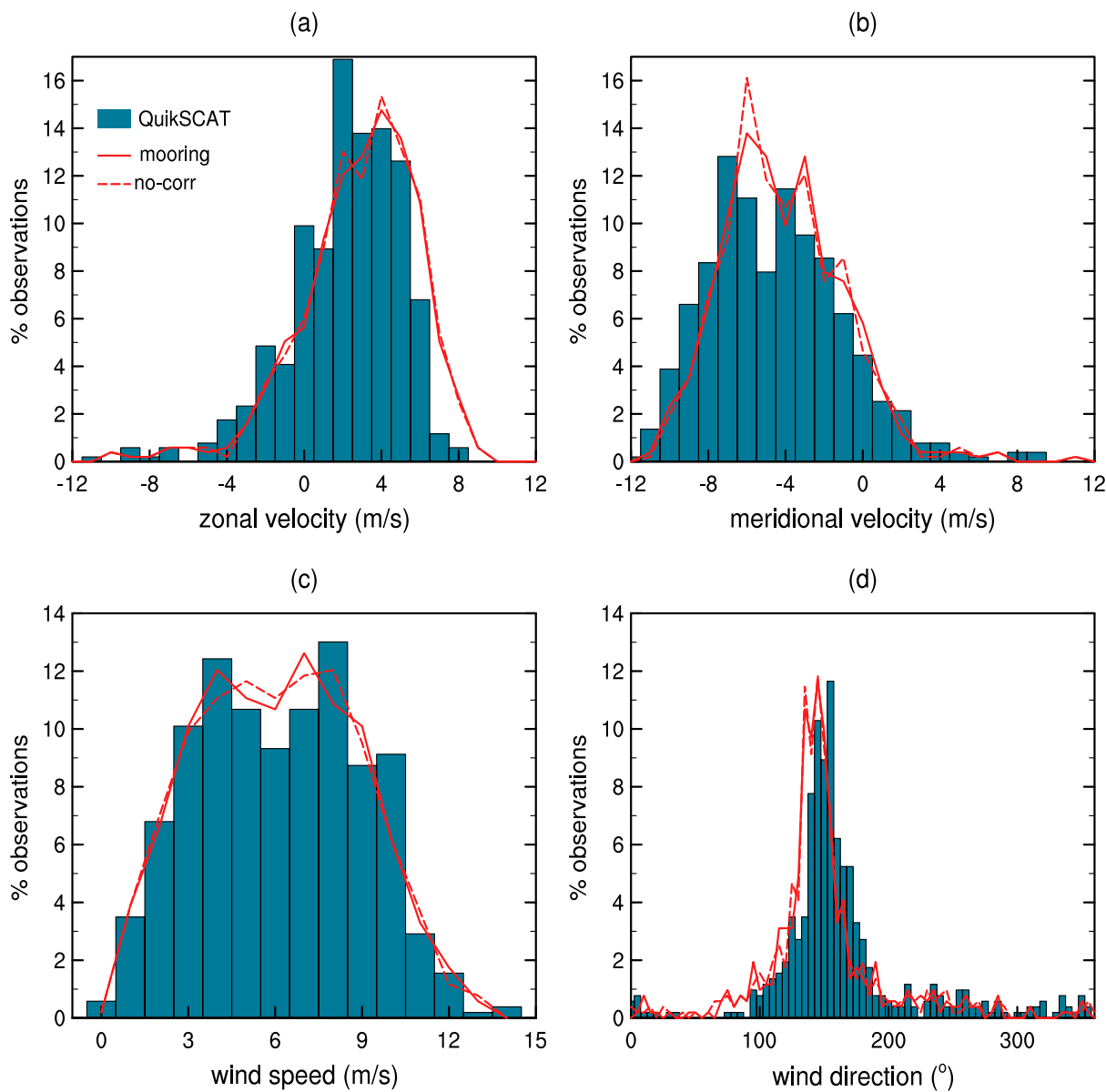


Fig. 6. Histograms from QuikSCAT winds (blue bars) and hourly-average in situ data (red curves) based on the collocated data: (a) zonal velocity (u); (b) meridional velocity (v); (c) wind speed and (d) wind direction. Histograms were computed using bins of 1 m/s for wind speed, u , v and 5° for wind direction. Vertical axes indicate the percentage of 515 collocated observations that fall in the respective bins. Solid red curves are used for in situ winds corrected for surface current effects and dashed curves for the data without correction. (For interpretation of the references to color in this figure legend, the reader is referred to the web version of this article.)

component points into the third quadrant at about 225° , while a wind that blows to the west points to 270° . Therefore, the adopted definition includes winds that are across the main axis such as the wind jet labelled as J2–J3 (235° – 245°) in Fig. 5a and winds that are almost-perfectly to the west such as the wind jet labelled as J1 ($\approx 261^\circ$) in the same figure. Hereafter, we refer to these events as westward wind events or cross-axis westward winds. The same wind direction criterion is used to determine the occurrence of westward events in the WHOI/KAUST mooring data.

Similar to Holbach and Bourassa (2014), the median wind direction in the eastern boundary (dashed area in Fig. 3a) is used to identify westward events. An event can have duration from one to several days, since the 3-day moving average QuikSCAT dataset has a daily time step. The wind speed can vary during an event, although the winds always have a negative zonal component and direction in the 215° – 280° range.

The procedure for identifying westward events is repeated for each latitude along the reference line individually. While the detection of a

westward event is based on the wind direction, the zonal velocity is used to pinpoint the dates when the events start/end. Westward winds, by definition, must have negative zonal component velocity $u < 0$. Here, we use $u = -1$ m/s as the threshold to define the start/end of an event. When two events occur close in time (< 2 days), we consider them as a single event.

Basic statistics by latitude are calculated such as the mean, minimum and maximum wind speeds and duration of each event. We also estimate the percentage area ($P_a(t)$) of the northern Red Sea over which the winds are westward as $P_a(t) = (A_{west}(t)/A_{NRS}) * 100$, where t is the time step (daily), $A_{west}(t)$ is the area cover by westward winds at time t and A_{NRS} is the northern Red Sea area. $A_{west}(t)$ is computed as the sum of the areas of all grid cells that have winds in the direction range of 215° to 280° . The area of a grid cell on a sphere is given by $A_{cell} = R^2 * \cos(y) * dx * 2 * \sin(dy/2)$, where R is the radius of Earth at the equator, y is latitude, dx and dy are the longitudinal/latitudinal grid resolutions, respectively. The northern Red Sea area (A_{NRS}) is computed

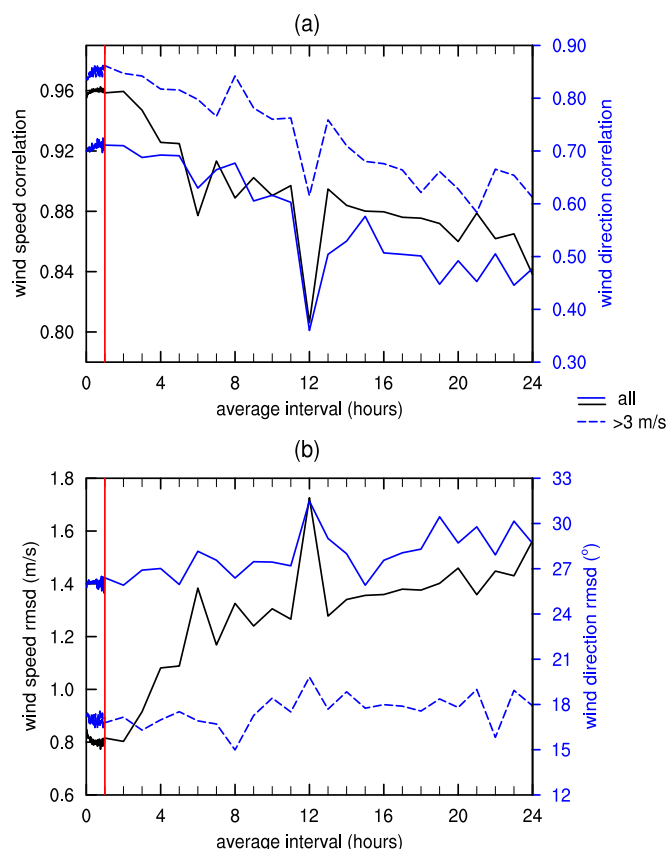


Fig. 7. Impact of the temporal averaging of in situ observations on the QuikSCAT/in situ collocation: (a) Linear correlation coefficients and (b) root-mean-square of the differences (*rmsd*). In situ winds are not corrected for surface current effects. Horizontal axes show the time averaging (1 min time-step below 1 h and 60 min above that). Left vertical axes and black curves are used for wind speed. Right axes and blue curves for wind direction. Solid curves show the statistics using all data and dashed curves for wind speeds > 3 m/s. Vertical red lines mark the one hour time average interval. (For interpretation of the references to color in this figure legend, the reader is referred to the web version of this article.)

as the sum of the areas of all grid cells between of 20° N and 30° N identified as sea. To identify sea/land grid cells, we use the ETOPO-2 bilinearly interpolated to the QuikSCAT grid. For comparison and as a measure of uncertainty, we estimate the area occupied by winds in the direction range of 221.5°–273.5° (20% narrower than the original interval).

Additionally, the meridional migration of the RSCZ is investigated because the presence of this zone can influence the mountain-gap wind statistics in the southern limit of our study area, since the winds are also westward under the RSCZ when this zone exists (e.g. Fig. 2 j–m). As a proxy for the RSCZ, we use the zero line of the meridional wind component, in which v is positive south of the line (southern Red Sea) and negative north of it (northern Red Sea). Here, the median position of this zero line is adopted as the RSCZ location. We choose this simple identification method based on the Pedgley (1966a) description (e.g., Fig. 3c) because the daily surface wind convergence fields ($-\partial u/\partial x + \partial v/\partial y$) exhibit other convergence areas with similar strength as the RSCZ. These convergence areas are not associated with the RSCZ wind pattern that we are interested in: opposite-blowing along-axis winds that meet at the central Red Sea and bend westward towards the Tokar Gap direction.

3.3. Large-scale cross-axis westward winds

Jiang et al. (2009) using a short term, high-resolution model simulation showed that stronger mountain-gap westward winds may

cover a large fraction (up to 40%) of the northern Red Sea for a couple of days. To examine the occurrence of this kind of event, we trace all events in QuikSCAT where the median winds in the eastern boundary are westward over 60% or more of the reference line ($> 4.3^\circ$ in latitude) and have duration at least of two days. During these events the westward winds are coherent over a large latitudinal range, encompassing several wind jets, such as the event shown in Fig. 5. We call them large-scale westward events.

We chose the threshold of 60% because in the event of 15 January 2009 westward winds cover about 70% of the reference line in QuikSCAT (Fig. 5a) and we want to determine the frequency of similar events. By adopting a large threshold (60%), we also avoid possible statistical contamination by narrow westward winds associated with the RSCZ: Compare Fig. 5 (large-scale westward winds) to Fig. 2 j–m (RSCZ). Nevertheless, we evaluate the effect of other threshold choices.

For a better understanding of the wind pattern and wind stress curl associated with these large-scale westward events, a composite analysis similar to Papadopoulos et al. (2013) is employed. Because composites involve the selection and averaging of key events, the stochastic variability can be reduced, increasing the signal to noise ratio. The composites return patterns that are more robust and statistically significant than the individual events.

To produce the composites, we first select wind and wind curl fields of each large-scale event. Because these events can have different durations (three to eight days as shown later), the selected field for each event is the field where westward winds cover the largest latitudinal range of the reference line. Then, the selected fields are averaged to construct the composite.

3.4. Determining the space-time variability of QuikSCAT winds

To assess the spatial structure and temporal variability of the QuikSCAT winds over the northern Red Sea in a broad sense, we perform four different real-vector Empirical Orthogonal Function (EOF) analyses. EOF is a well-known statistical technique based on the covariance structure of the dataset. It is expressed through an orthogonal series of dominant statistical modes, obtained with no priori assumptions on either spatial or temporal behavior of the input data (e.g., Bjornsson and Venegas, 1997; Emery and Thomson, 2001; Kaihatu et al., 1998, and references therein). In general, the first few EOF modes are enough to explain most of the dataset variance. Vector EOF analyses are widely used in meteorology to extract the dominant modes (in a statistical sense) of the wind fields (e.g., Kaihatu et al., 1998; Ludwig et al., 2004). As described by Kaihatu et al. (1998), two vector EOF analysis approaches can be employed. One approach is referred to as complex EOF analysis, which uses complex scalars from u, v components of the vector field, and the other is called real-vector EOF, which leaves the vector structure intact. Kaihatu et al. (1998) have compared both approaches and found the real-vector method better at avoiding directional ambiguity. Broadly speaking, the real-vector EOFs are computed from an extended data matrix formed by appending the v to the u component data, after the temporal mean (e.g., long-term or annual cycle) of each component has been removed. Details can be found in Kaihatu et al. (1998).

The time series of the EOF decomposition (principal components, PCs) are further analysed to characterize the temporal variability associated with the spatial patterns. To quantify the relative variance associated with an EOF mode at different time scales, we performed a Singular Spectrum Analysis (SSA) associated with the Maximum Entropy Method (MEM) since these methods are well-suited for finite time series (Ghil et al., 2002). SSA is a data-adaptive technique designed to extract information from short, noisy time series containing modulated oscillations and trends. Using the SSA decomposition, each PC is projected into 5 bands of temporal variability using a number of Reconstructed Components (RC) equivalent to 99% of the PC variance (e.g., Vianna and Menezes, 2006; Vianna and Menezes, 2013; Menezes

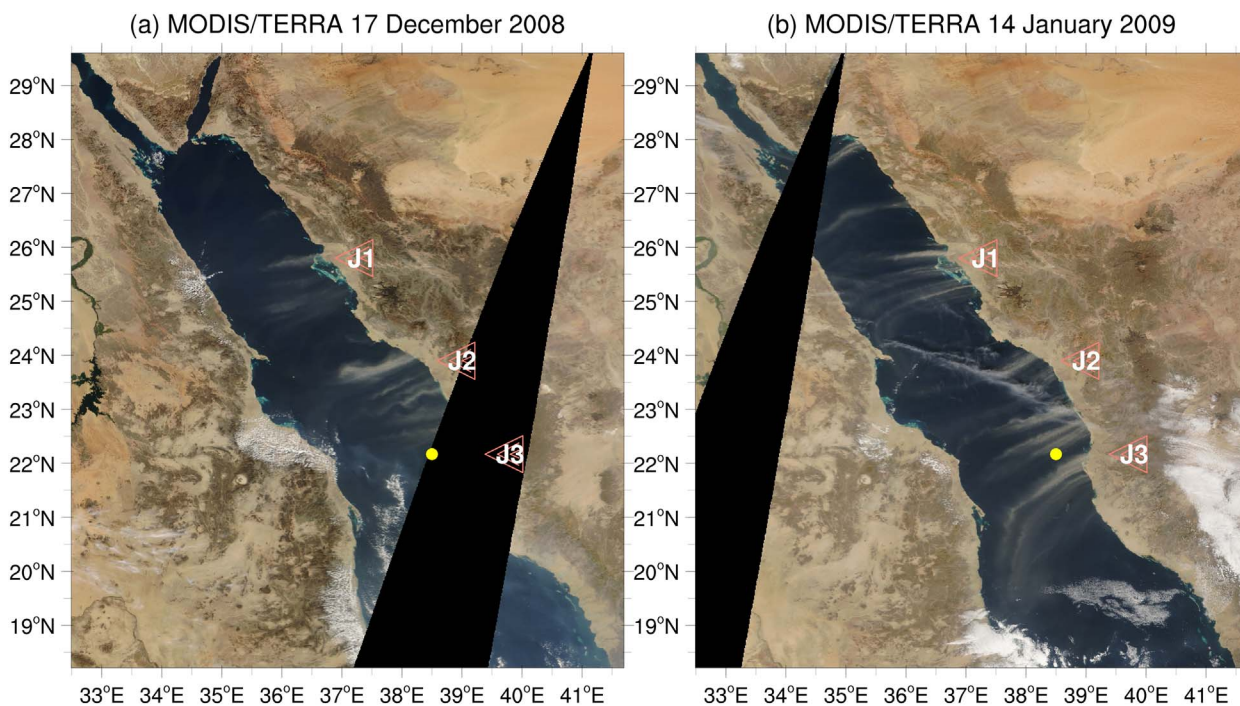


Fig. 8. True color composite images from MODIS/TERRA satellite during two westward wind jet events: (a) 17 December 2008 (b) 14 January 2009. Yellow dot shows the WHOI/KAUST mooring position. Left pointed triangles indicate the position of the three main wind jets identified in the WRF simulation (J1, J2 and J3). Both MODIS images have 125 m spatial resolution. (For interpretation of the references to color in this figure legend, the reader is referred to the web version of this article.)

et al., 2014; Menezes et al., 2016). Here, the bands are denoted as intraseasonal ($T \leq 150$ days), semi-annual ($150 < T \leq 210$ days), quasi-annual ($210 < T \leq 340$ days), annual ($340 < T \leq 438$ days) and interannual ($T > 1.2$ years). The SSA decomposition is performed using a value of M (free window parameter) of $N/3$, where N is the length of PC time series (see Ghil et al., 2002; Vianna and Menezes, 2006; Vianna and Menezes, 2013, for details). In addition, the intraseasonal band (≤ 150 days) of each PC, which in general explains a large part of the PC variance, is analysed with MEM to determine the main spectral periods in that band. The purpose of this latter analysis is to find out if the spectra of the EOF modes exhibiting cross-axis winds have peaks at about 10–20 days. Based on a short-term simulation, Jiang et al. (2009) suggested that the westward wind events occur at this interval in winter. But, we make no attempt to investigate the intraseasonal band in the present work because many weather phenomena besides the wind jets can occur in this band and our focus here is on the mountain-gap wind characteristics.

Similar to Jiang et al. (2009), the wind variability is also evaluated through the directional wind steadiness parameter. The wind steadiness is given by the ratio of the mean vector velocity to the mean scalar speed, and values near one mean that the wind direction has remained steady over the averaging period (Singer, 1967). To compute the steadiness parameter, we use the 3-day moving average product and an averaging period of one month, as was done by Jiang et al. (2009).

4. Results

4.1. Evaluation of the QuikSCAT winds

QuikSCAT winds agree well with the collocated hourly averaged in situ winds measured at the WHOI/KAUST mooring (Table 1). The linear correlation coefficient between the 515 collocated observations is 0.96 for wind speed, 0.72 for wind direction and 0.89/0.88 for u/v . Bias in wind speed is negligible, but for wind direction is about 15° (clockwise). Taking only the collocated pairs for in situ winds above 3 m/s (QuikSCAT range), the bias in direction reduces to 11.8° and correlation

increases to 0.85. The root-mean-square difference (*rmsd*) also decreases from 25.6° to 17.4° , which is better than the QuikSCAT target accuracy of 20° . For wind speed, there is no difference in correlation coefficient in the two cases. The statistics are slightly worse with no correction for surface currents if the full wind speed range is considered (not shown) but for winds stronger than 3 m/s there is no difference with or without correction.

In terms of wind components, QuikSCAT collocated measurements underestimate the zonal velocities u by about 0.8 m/s. This occurs because there are fewer observations with $u > 6$ m/s in QuikSCAT as shown in the histograms of Fig. 6a, which is independent of the surface current correction for the in situ data. For negative zonal velocities, i.e. the westward winds we are interested in, QuikSCAT presents a similar statistical distribution to the mooring. In QuikSCAT, 15.3% of the data have westward velocities stronger than -1 m/s, which is only slightly larger than the in situ proportion (12.6%). Despite the mean direction being displaced by about 10° in QuikSCAT, the statistical distributions of in situ and satellite winds are similar in the mountain-gap wind jet range (215° – 280°), with 7% (in situ) and 8% (QuikSCAT) of the collocated data falling in this range (Fig. 6d). For meridional velocity and wind speed, the QuikSCAT histograms resemble the mooring (Fig. 6b–c).

The agreement between QuikSCAT and in situ winds is also robust for other in situ time-average intervals. Correlations are highest and *rmsd* are lowest for averaging periods of < 80 min (Fig. 7). The best correlations and *rmsd* are found between 46–58 min for all variables (u, v , wind speed and direction). This interval is near to the hourly-average in situ data analysed above. Even if we consider larger intervals (up to 3 h), the correlations and the *rmsd* are still good. For time intervals above 4 h, correlations decrease and *rmsd* increase (with minima around 12 h), which is not surprising given the strong semi-diurnal and diurnal cycles associated with the land-sea breezes in the Red Sea.

Despite the moderate spatial resolution of QuikSCAT (25 km) when compared with the Red Sea width of about 400 km, QuikSCAT captures relatively well the basin-scale pattern of the northern Red Sea westward wind jets. For example, Fig. 5 shows a QuikSCAT pass on 15 January

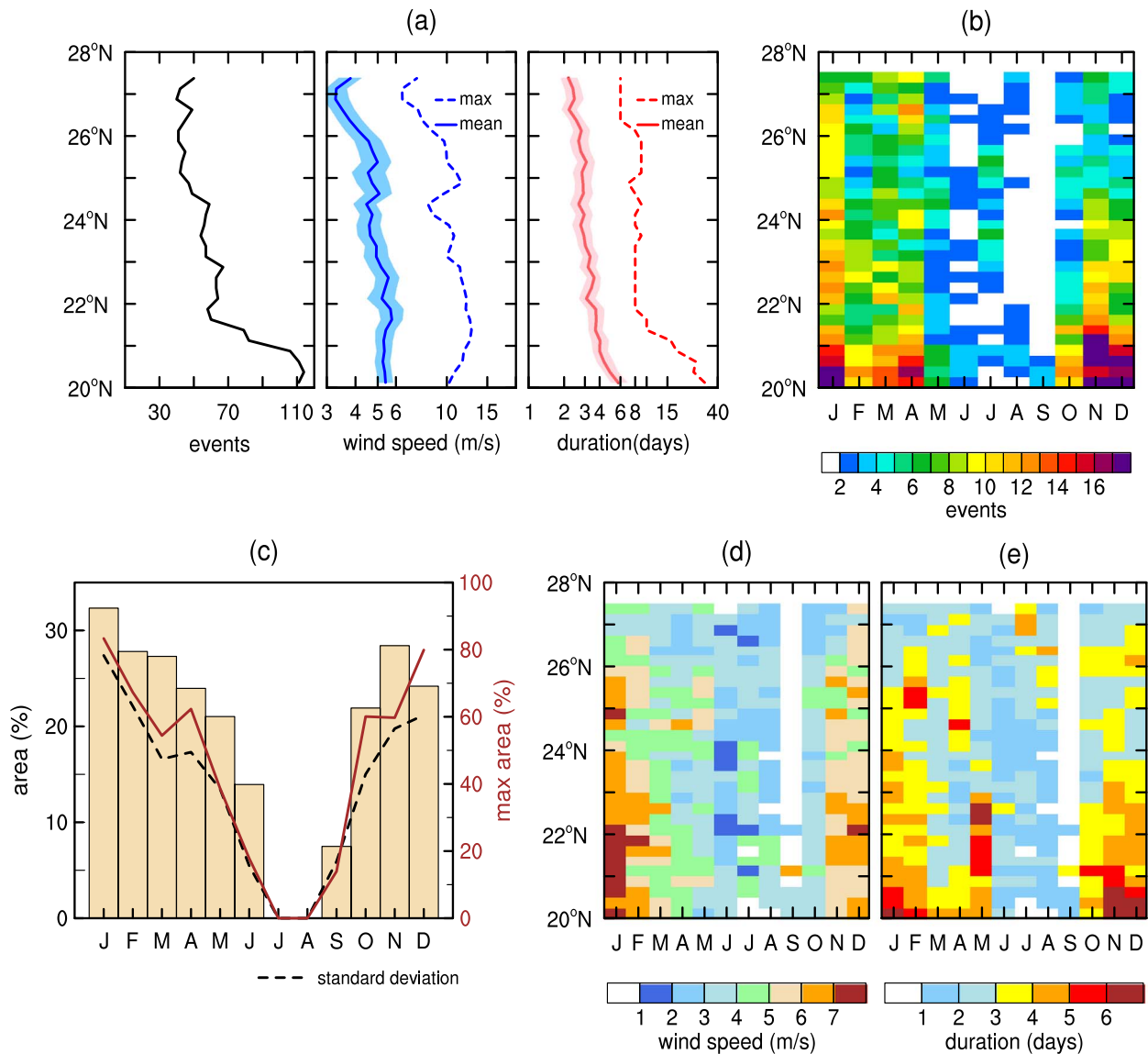


Fig. 9. Statistics of westward wind events (215°–280°, oceanographic convention) over the eastern boundary region. (a): number of events in ten years by latitude (left), the respective mean/maximum wind speeds (middle) and mean/maximum duration (right). Shadings show the 95% confidence intervals on the means estimated using the bias-corrected and accelerated bootstrap method with 1000 samples. (b): seasonal distribution of number of events by latitude. (c): seasonal distribution of the area covered by westward winds. Values are given in percentages relative to the northern Red Sea area. Bars show the mean area and dashed curve is the standard deviation, both using the left vertical axis. Brown curve shows the maximum area at each month and uses the right-vertical axis. (d) and (e): seasonal distribution of the wind speed and duration of the westward events, respectively. White indicates no-event. (For interpretation of the references to color in this figure legend, the reader is referred to the web version of this article.)

2009 around 0300 AM UTC and the respective wind field from the 10-km spatial resolution simulation of Jiang et al. (2009). North of 20° N, there are three main westward wind jets in the simulation, with speeds of 12–15 m/s (left-pointed triangles in Fig. 5b). These wind jets are located where the mean elevation of the Hijaz-Asir Mountains is lowest (< 400 m above sea level) (Fig. 3b). In the QuikSCAT map, the wind jets have similar magnitudes but only two main individual jets can be identified. The jets labelled as J2 and J3 appear merged together in QuikSCAT, probably because the spatial resolution of QuikSCAT is too coarse to resolve these two wind jets separately. The separation, i.e. the region with lower speeds between the jets, is about 25–30 km in the simulated wind field, which is of the order of QuikSCAT spatial resolution. Between the southern jets and the northern ones located at 25° N–26° N, the separation is larger (≈ 75 km), and the northern jet appears as an individual jet in the QuikSCAT map. As shown by Jiang et al. (2009), in true-color MODIS (Moderate Resolution Imaging Spectroradiometer) images the dust from the desert can act as a tracer

of the westward winds. The database from the NASA GSFC (Goddard Space Flight Center) MODIS Rapid Response Team has several images of dust storms associated with wintertime mountain-gap westward winds (e.g. Fig. 8). Most images show narrow jet-like features such as Fig. 8 and Fig. 3c of Jiang et al. (2009), instead of a broad jet as shown by QuikSCAT.

QuikSCAT jets also tend to be less zonal than the simulated ones, especially the wind jets between 21° N–24° N. In this region, the mean difference in direction between QuikSCAT and WRF is 16.7° (*rmsd* of 13.08°). Indeed, the QuikSCAT jet direction agrees better with in situ observations. For example, the wind jet direction at the mooring location is 237° in the QuikSCAT morning pass and the collocated in situ wind has direction of 238.2°/235.9° (with/without sea surface current correction). In the WRF, the wind direction at the mooring location is 273.9°, about 40° clockwise in relation to the in situ observation. For the northern jet (25° N–26° N), the bias and *rmsd* between QuikSCAT and WRF are smaller (5.89°; 3.23°), with both showing a quasi-zonal jet.

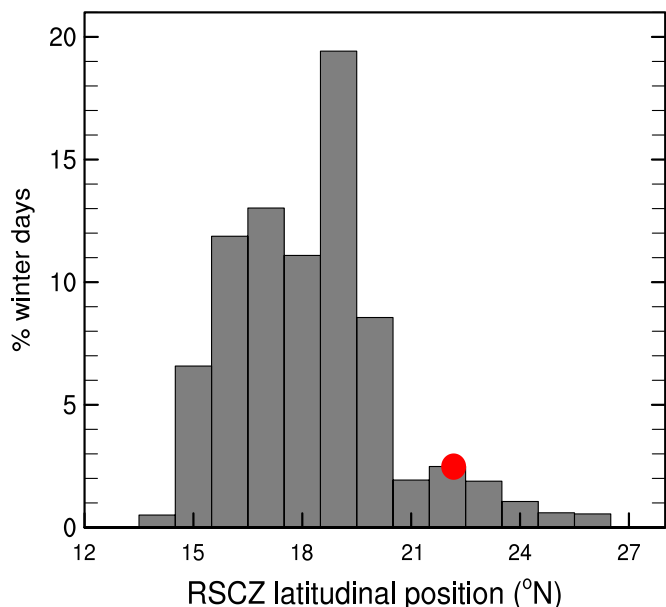


Fig. 10. Histogram of the RSCZ position during the winter monsoon season (October–April) in QuikSCAT. Vertical axis is the percentage of the winter monsoon days (2173 days) in which the RSCZ is over the latitude given by the bins (horizontal axis). Bins have 1° width. Red dot shows the WHOI/KAUST mooring position. Notice, in 20% of the winter days, there is no RSCZ. (For interpretation of the references to color in this figure legend, the reader is referred to the web version of this article.)

4.2. Westward wind events: statistics

Westward wind events are relatively common in the northern Red Sea as seen by QuikSCAT, with about 50–70 events north of 21.5° N in 10 years (Fig. 9a, left). South of this latitude, westward winds are more frequent (70–110), which reflects much more the presence of the RSCZ in this region than the mountain-gap wind jets since the Asir Mountains are closely compacted there with elevations above 2000 m (Fig. 3a). In the winter monsoon season (October–April), the RSCZ is located 41% of the winter days over the region between 18° N–21° N (Fig. 10). South of 21.5° N, the westward events are not only more frequent but also have longer mean duration (about six days) due to the RSCZ presence. For instance, in this region QuikSCAT recorded westward winds lasting

Table 2

Statistics of westward wind events (215°–280°, oceanographic convention) at the WHOI/KAUST mooring (22.17° N; 38.5° E). First column is the event number (temporal order), second column shows the start date, third column is the event duration, fourth and fifth columns are the mean and maximum wind speeds during the event, respectively.

Evt	Start	Duration (days)	Mean speed (m/s)	Max speed (m/s)
01	2008-12-03	5	6.9	9.1
02	2008-12-17	6	7.7	11.8
03	2009-01-14	4	6.9	10.0
04	2009-10-23	4	1.4	2.3
05	2009-12-02	2	2.1	2.5
06	2009-12-24	2	4.6	5.3
07	2010-01-02	2	2.9	5.2
08	2010-01-07	11	4.9	8.5
09	2010-01-29	5	2.4	4.3
10	2010-03-09	8	2.5	5.1
11	2010-04-03	3	2.9	3.9
12	2010-10-19	3	2.9	4.5
13	2010-11-11	3	2.8	5.5
14	2010-11-23	14	4.3	9.3

from 10 to 31 days (Fig. 9a, right). Events persisting for 31 days occurred twice at 20.375° N in the QuikSCAT record, with maximum speeds of 7.58 m/s (10/22/2004 to 11/21/2004) and 8.01 m/s (11/25/2005 to 12/25/2005). During these long-lasting westward events, the RSCZ position was between 19° N–21° N for 48.4% and 83.9% of the event duration, respectively. Therefore, the increased number of westward wind events in the latitudes south of 21.5° N reflects the mountain-gap wind jets plus the RSCZ-associated westward winds.

Outside the region influenced by the RSCZ, the wind speed and duration of the westward events decrease northward (Fig. 9a, middle and right). The events are on average longer at 22° N (3.5 days) and shorter at 27° N (2 days). The time-average wind speeds vary from 3 m/s (27° N) to 5.5 m/s (22° N) and maximum speeds reach above 10 m/s.

The westward events occur in winter, preferentially from November to January in most latitudes (about 10–12 events north of 22° N) (Fig. 9b). On average, a westward event covers 25–30 % of the northern Red Sea area during winter (Fig. 9c, bars), but the maximum area can be as large as 80% in December and January (brown curve in the same figure). There is a large variability between events in terms of area as indicated by the high standard deviation (Fig. 9c, dashed curve).

In relation to the wind speeds, the events are stronger in January (about 6 m/s) and slightly weaker in November (5 m/s)

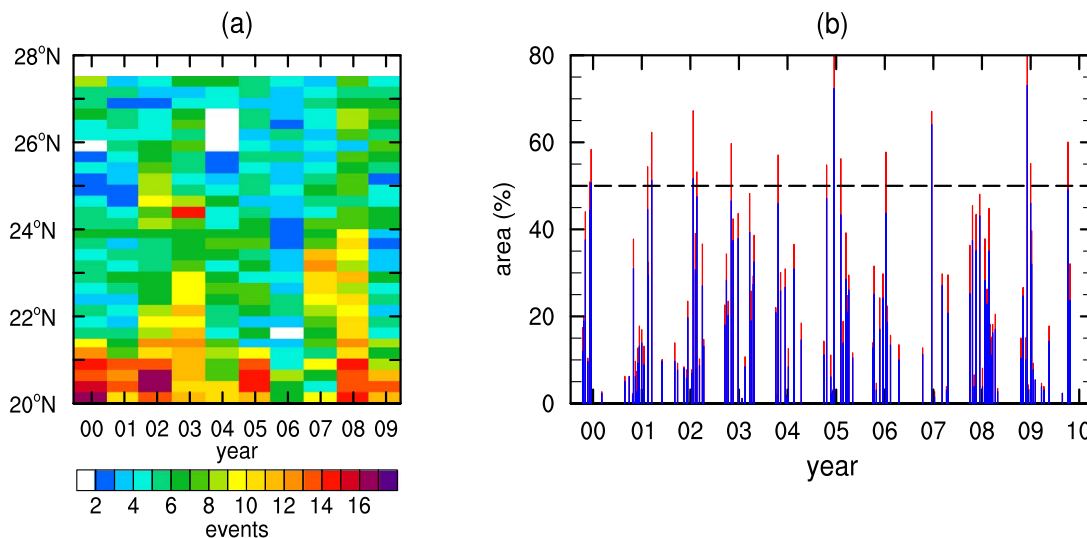


Fig. 11. (a): Number of westward events at each year (2000–2009) by latitude. (b): Time series of the maximum area of the northern Red Sea covered by westward winds (215°–273°) during wind jet events (red bars). Blue bars show similar areas but for winds in the direction range of 221.5°–273° (see text for details). Black dashed line indicates 50% of the northern Red Sea area. (For interpretation of the references to color in this figure legend, the reader is referred to the web version of this article.)

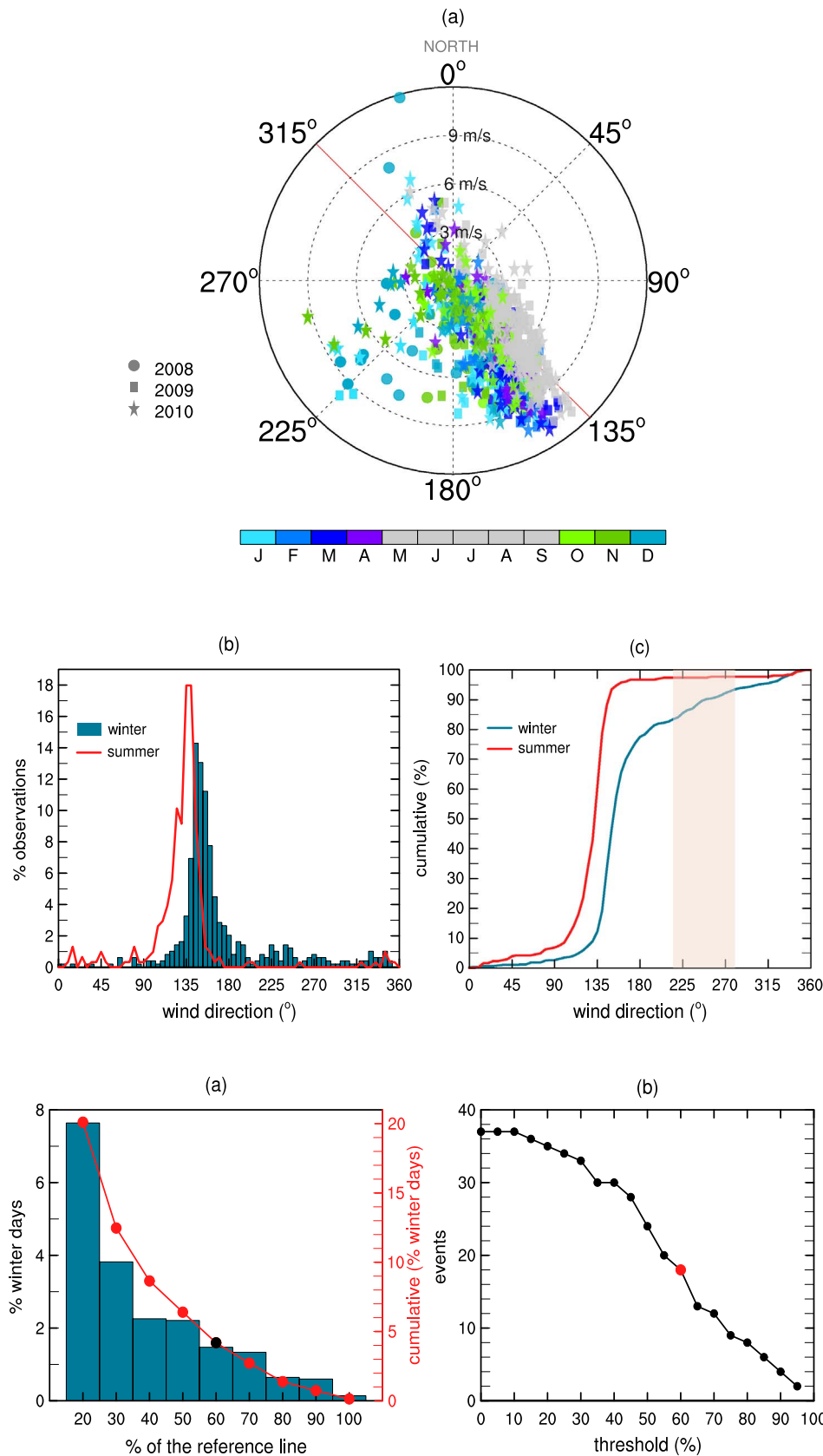


Fig. 12. (a) Winds at the WHOI/KAUST mooring (22.17° N; 38.5° E) between 12 October 2008 and 16 December 2010. Radial lines show wind direction (oceanographic convention), concentric circles are wind speeds (m/s), each symbol represents a daily-average value where the color indicates the month (bottom colorbar) and the shape indicates the year (left legend). Red line is approximately the inclination of the northern Red Sea main axis. (b) Histograms of wind direction for the summer (May–September) and the winter (October–April) monsoons at the WHOI/KAUST mooring (same period as (a)). Histograms were computed using bins of 5°. The vertical axis indicates the percentage of observations that fall in the respective bin and is given in relation to the total observations in summer (306 days) and winter (490 days), individually. (c) Same as (b) but cumulative histograms (from 0° to 360°). Shading highlights the westward wind jet directional range. There are (almost) no westward winds in summer. (For interpretation of the references to color in this figure legend, the reader is referred to the web version of this article.)

Fig. 13. (a) Statistical distribution of westward winds over the eastern boundary during the winter monsoon (October–April). Vertical axes give the percentage of days in winter and the horizontal axis is the percentage of the reference line covered by westward winds (215°–280°). We show only the portion of the histograms where westward winds cover more than 20% of the reference line (> 1.45° in latitude). The standard histogram is the blue bars using the left axis; the cumulative histogram (integrated from right to left) is the red curve using the right axis. Black dot highlights the 60th percentile. (b) Number of westward events with duration larger than two days using different thresholds. Red dot highlights the 60th percentile (18 events). (For interpretation of the references to color in this figure legend, the reader is referred to the web version of this article.)

(Fig. 9d). During winter, typical duration is 3–4 days north of 22° N, and 7 days south of this latitude (Fig. 9e). South of 23° N, the events have longest duration in May (5 to 7 days).

Although westward winds are a typical winter phenomenon, some

events are detected in summer, especially in July north of 22.5° N (Fig. 9b). However, in the summer events, the winds are weaker (Fig. 9d), the duration is usually shorter (Fig. 9e), and cover a smaller area (Fig. 9c).

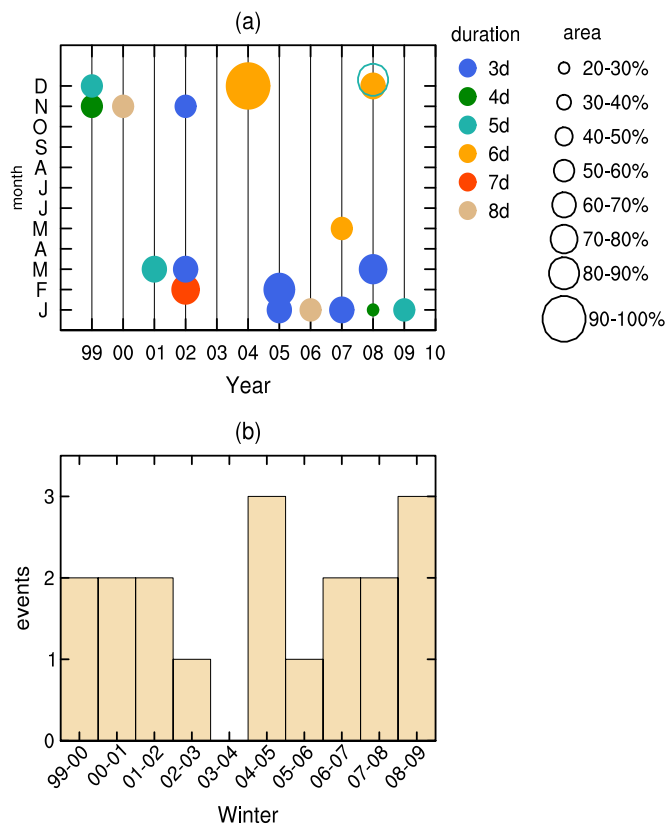


Fig. 14. (a) Statistics of large-scale westward events in QuikSCAT over the northern Red Sea. Vertical axis (y) gives the month (January to December) and the horizontal axis (x) the year (1999–2009). Color and size of the symbols indicate the event duration in days and maximum reached area, respectively, using the legend on the right. For example, QuikSCAT recorded in 2004 (x-axis) one large-scale event (one dot) that occurred in December (y-axis), have duration of 6 days (dot color, yellow) and covered 90%–100% of the northern Red Sea (dot size-largest). Area is given in %, which represents the area covered by winds with direction between 215°–305° in relation to the entire northern Red Sea area. Rings are used when two events occur in the same month. (b) Number of large-scale westward events by winter monsoon season. (For interpretation of the references to color in this figure legend, the reader is referred to the web version of this article.)

QuikSCAT also shows the westward events having strong inter-annual variability, with the events being more frequent in 2002–2003 and 2007–2008 in most latitudes (yellowish in Fig. 11a). In these years, there are 8–10 events north of 22° N. In contrast, two to four events occur in 2006 for all latitudes north of 20.5° N. Interannual variability is also reflected in the area of the northern Red Sea covered by westward winds (215°–280°) (Fig. 11b, red bars). For example, in 2008 there is no event covering more than 50% of the northern Red Sea area although 2008 has the largest number of events (Fig. 11a). In all other years, there are events covering an area larger than 50%. In the QuikSCAT record, the largest numbers of widely-extended events occur in 2005 (Fig. 11b). If we consider winds from a narrower interval (221.5°–273.5°), the interpretation is essentially the same (blue bars in Fig. 11b). The mean difference in area between the two westward wind classifications is only 4.5% and the *rmsd* is 3.6%.

In summary, cross-axis westward winds are more common in winter and have strong interannual variability. Near the southern limit of our study area, the westward wind statistics reflect the occurrence of both dry mountain-gap wind jets and moist winds associated with the RSCZ.

Applying the same methodology as used for the QuikSCAT data, 14 westward events are detected in the in situ measurements (Table 2). The in situ westward winds mostly occur between November and January (Fig. 12a), consistent with the longer QuikSCAT record. Winds during the summer monsoon (May–September) are mostly unidirectional, southward along the Red Sea main axis. Westward winds are

rare in summer: only 0.3% of the summer monsoon wind observations fall in the 215°–280° range at the WHOI/KAUST mooring, and no westward winds stronger than 3 m/s are detected in this season (Fig. 12). In contrast, in winter the winds more frequently have a westward component (180° < direction < 360°), with about 11% of the winter observations falling in the 215°–280° range (Fig. 12b–c). The westward winds captured by the mooring are very likely to be mountain-gap wind jets since only 2.6% of the winter days, the RSCZ is near the mooring (21.5° N–22.5° N) according to QuikSCAT (Fig. 10).

The westward events measured at the WHOI/KAUST mooring have duration varying from 2 to 13 days (Table 2), and frequency (≈ 6.3 events/year) similar to those found in QuikSCAT at 22° N (about 6.5 events/year). The largest number of events is found in December and January, with four events occurring in each month. The mean wind speeds vary from 1.4 m/s to 7.7 m/s and maximum reaches 11.8 m/s, in the same range as the QuikSCAT data. Year-to-year difference is also observed in the mooring data. For example, there are four events in 2009 and eight in 2010. In 2010, the events are also longer with two events lasting for more than 10 days (Table 2, events 8 and 14).

4.3. Large-scale cross-axis westward wind events

During the winter monsoons (October–April), westward winds in QuikSCAT cover more than 20% of the reference line in 20% of the days (Fig. 13a). Westward winds covering more than half of the northern Red Sea are less frequent (7%). Large-scale events (> 60% of the reference line), similar to the 15 January 2009 event, happen in 4% of the winter days. In this section, we focus on these large-scale westward events. For comparison, Fig. 13b shows the number of westward events with duration of more than two days as a function of different thresholds defining large-scale events. As might be expected, the number of events decrease almost linearly with the threshold: there are 24 events covering more than 50% of the reference line in ten years and only eight events covering more than 80%.

QuikSCAT recorded 18 large-scale westward events (60% of the reference line) over the northern Red Sea during its 10-year lifetime (Fig. 14a). Large-scale westward events are more frequent in January (5 events) and December (4 events), with duration varying from 3 to 8 days. Duration here expresses the westward wind persistence in QuikSCAT data at the latitude of the WHOI/KAUST mooring (22.17° N). Except for one weak event in May (Figs. 14a and 15a), all events occur between November and March. Typically, the large-scale events occur 50–60 % of the northern Red Sea area, but some events can cover almost the entire basin as for example in December 2004 (Fig. 14a).

The event of December 2004 is not only the largest in terms of area, but it is also very strong with wind speeds about 9–10 m/s (90th percentile) and has relatively long duration (6 days). During this event, cross-axis winds extend from 18° N to 28° N (Fig. 15b), with almost all vectors having a westward zonal component in this region. The smallest event in terms of area occurred in January 2008 (20–30 % of the northern Red Sea). In spite of that, when we look at QuikSCAT fields during this event, we can identify at least two jets, one between 20° N and 23° N with speeds of 8–9 m/s, and another between 25° N–26° N (7–8 m/s) (Fig. 15c), both jets occurring offshore of mountain gaps.

Year-to-year difference is also clear in Fig. 14a. The largest number of events occur in 2008 (4 events) followed by 2002 (3 events). There were no large-scale events in 2003, and in 2001 and 2005 the large-scale events are weaker (3–5 m/s). It is interesting that there is no large-scale event in 2003 because a lot of westward events occur in this year (Fig. 11a) but none covering more than 60% of the reference line. If we arrange the large-scale events by winter, there are two of these events per season in general, with maximum of three large-scale events in 2004/2005 and 2008/2009 and no large-scale event in 2003/2004 (Fig. 14b).

Fig. 15d shows the wind vector composite (average) of all 18 large-scale events. As expected, the composite cross-axis winds are weaker

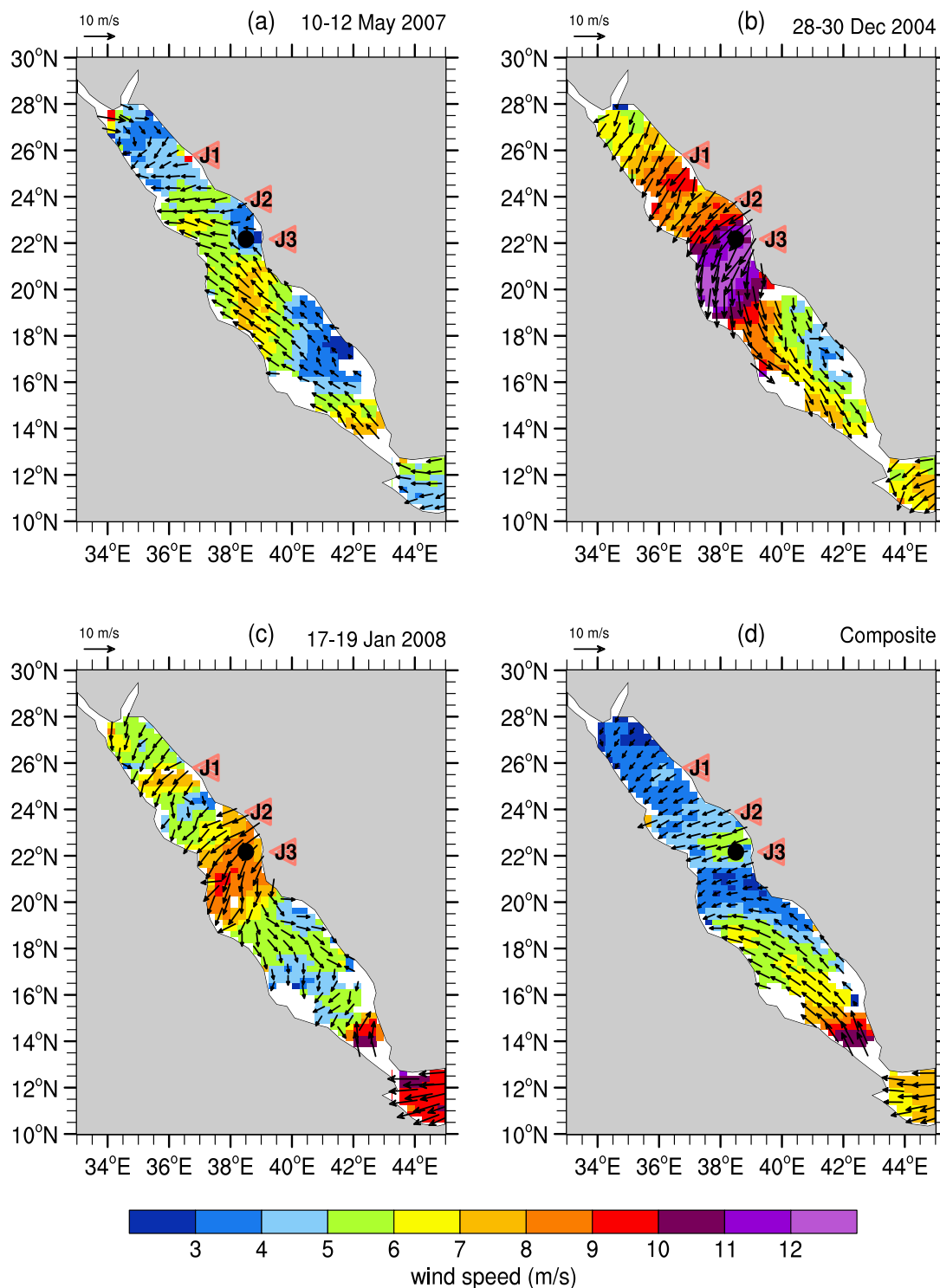


Fig. 15. Large-scale westward wind events. In (a–c): 3-day QuikSCAT wind fields. In (d): QuikSCAT wind field composite of the 18 large-scale westward events. Colors are the wind speed and vectors give the wind direction. For display purposes, vectors are shown with a coarsened resolution (approximately 0.56°). Black dot shows the WHOI/KAUST mooring position. Left pointed triangles indicate the position of the three main wind jets identified in the January 2009 event. (For interpretation of the references to color in this figure legend, the reader is referred to the web version of this article.)

(4–6 m/s) than the 3-day wind fields (5–12 m/s) (e.g., Fig. 15 a–c). In the large-scale event composite, the winds blow in a cross-axis direction over most of the northern Red Sea, with two regions with slightly enhanced wind speeds one between 22°N – 23.5° and another between 25°N – 26°N , which are the same regions where the jets were identified before. In the southern Red Sea, the winds are northward in the composite, but southward winds can also occur during westward

events. For example, Fig. 15b and c shows southward winds over the southern Red Sea, with no RSCZ, during two westward events (December 2004 and January 2008).

4.3.1. Wind stress curl

The wind stress curl associated with the large-scale westward events is characterized by a banded pattern of positive and negative values

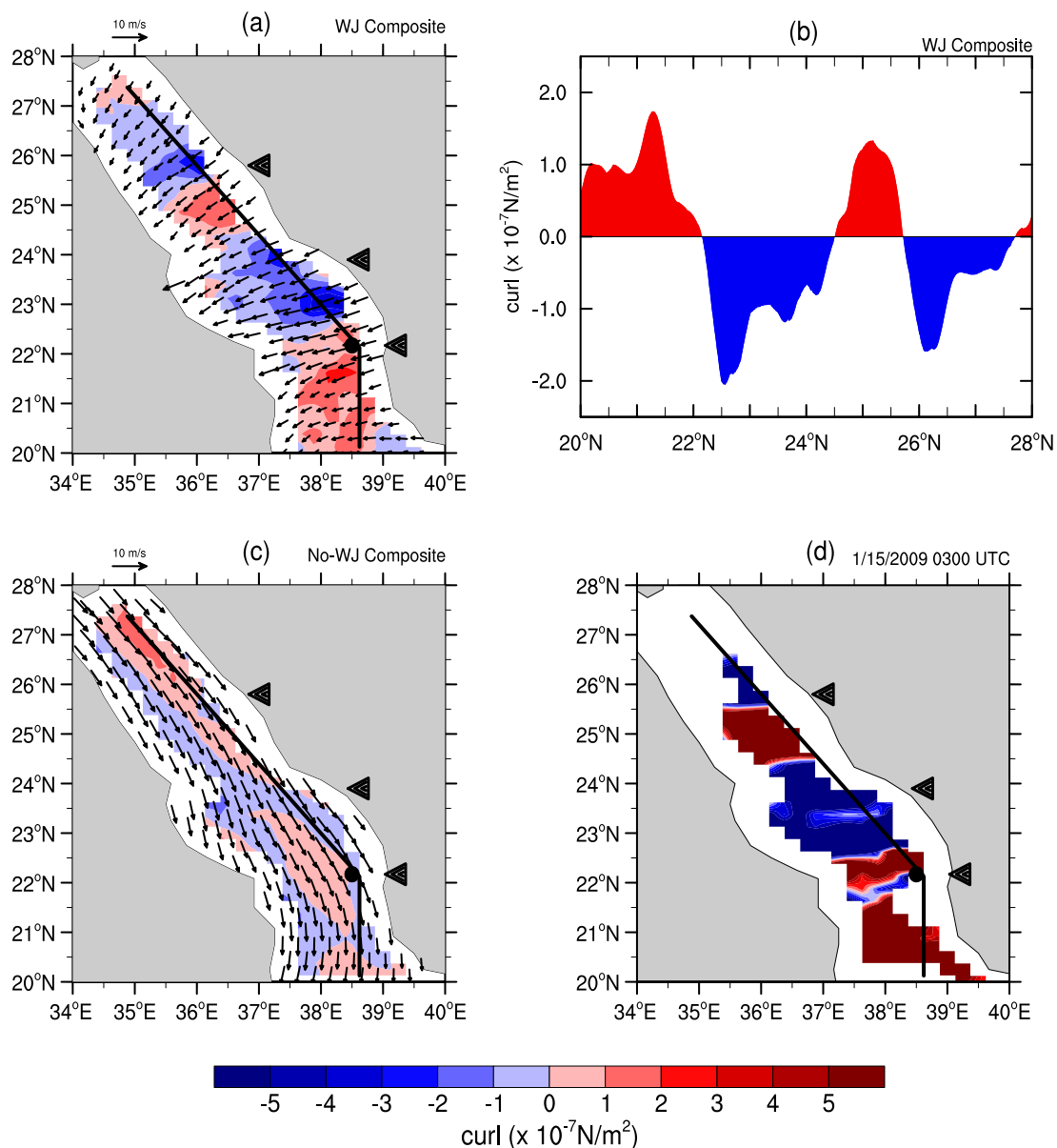


Fig. 16. Wind stress curl: (a) Composite of the large-scale westward events; (b) Cross-axis mean from the composite field. Red is used for positive curl and blue for negative; (c) Winter composite (November–January) excluding all large-scale westward events; (d) A snapshot based on the wind field of 15 January 2009 0300 UTC shown in Fig. 5a. Because there are several missing data in the snapshot north of 26° N, it was not possible to estimate the curl in that region. All maps use the same colorbar. For display purposes, vectors are shown with a coarsened resolution (approximately 0.45°). The black line is the reference line and the black dot shows the WHOI/KAUST mooring position. Left pointed triangles indicate the position of the three main wind jets identified in the January 2009 event. (For interpretation of the references to color in this figure legend, the reader is referred to the web version of this article.)

along the northern Red Sea main axis (Fig. 16a). Hereafter, maps focus on the northern Red Sea to highlight the spatial pattern in this area. Unfortunately, information near the coast is lost when the wind stress curl fields are computed (white around the northern Red Sea in Fig. 16a) because the QuikSCAT winds are only defined 15–30 km off the coastlines and we are using centered difference to estimate the derivatives. The positive/negative curl pattern along the main axis is evident in the wind stress curl averaged across the axis (Fig. 16b) and better defined and much stronger in the ascending/descending pass snapshots such as on 15 January 2009 0300 UTC (Fig. 16d).

The curl pattern of the large-scale westward events is very distinct from the winter climatological pattern associated with along-axis winds. In the latter case, the curl is predominantly positive (upwelling favorable) in the eastern side of the basin, along the Saudi Arabian coast, and negative in the western side (Fig. 16c), whereas the large-scale westward events produce a meridional sequence of positive and

negative values.

4.4. EOF analysis: revealing a cross-axis wind mode

About 80% of the wind variability over the northern Red Sea is explained by four EOF modes in QuikSCAT. The leading mode accounts for 55.8% of the variance and its spatial pattern resembles the mean field, with the winds blowing along the main axis (Fig. 17a). This mode can be interpreted as the strengthening/weakening of the south-eastward along-axis winds. The associated PC (Fig. 18a) is dominated by intraseasonal variations, with low variance in the annual band (Table 3). The intraseasonal band has one main spectral peak at 82 days. Large negative values in PC-1 are found in winter, which suggests that the along-axis winds may even blow opposite to the climatological direction. An inspection of the QuikSCAT wind fields confirms this interpretation. There are several times during winter in

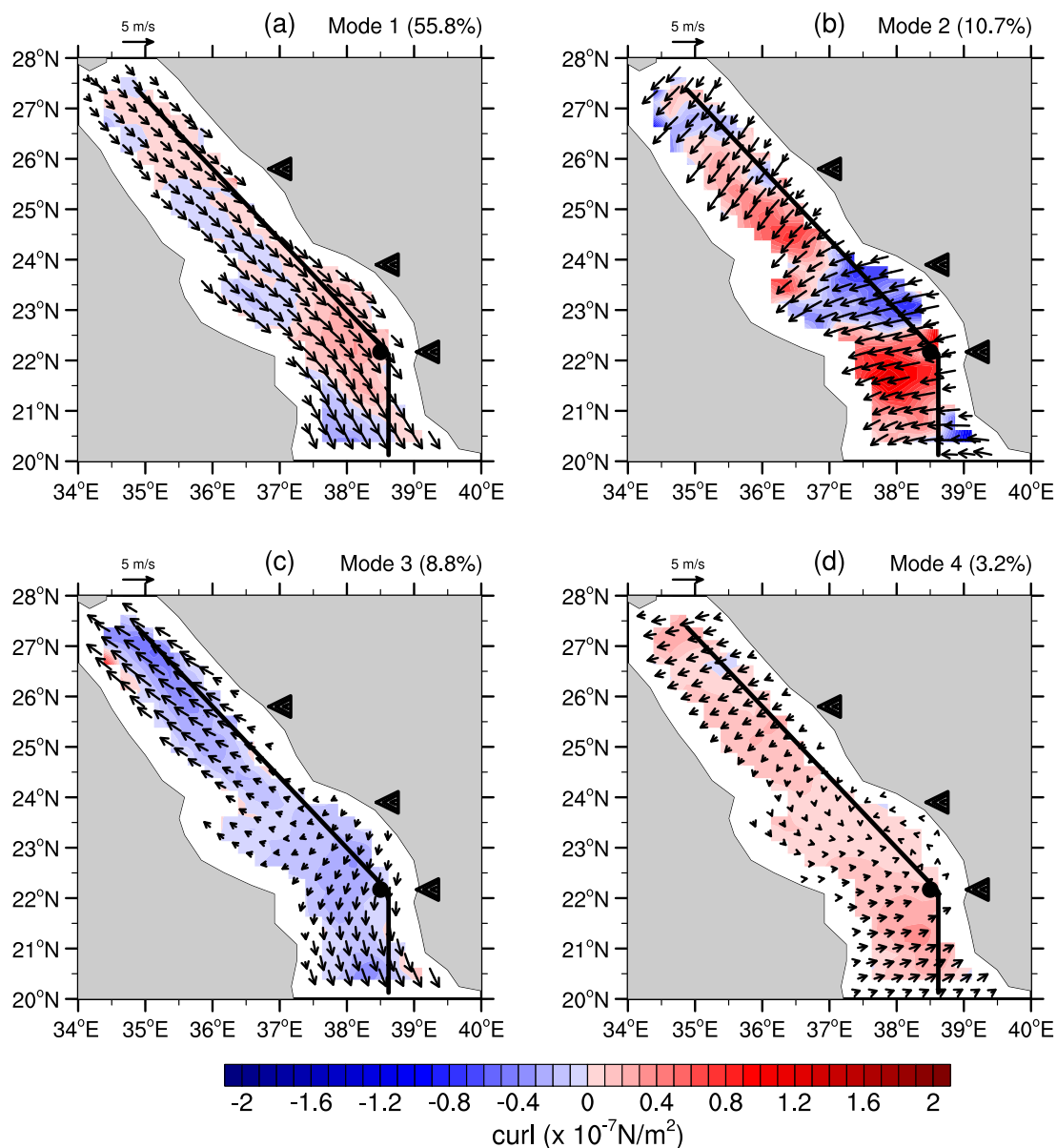


Fig. 17. The first four EOF spatial patterns (vectors) from QuikSCAT (07/20/1999–11/19/2009). Colors are the respective wind stress curls (see text for details). Percentages between parenthesis indicate the explained variance by each mode. The black line is the reference line and the black dot shows the WHOL/KAUST mooring position. Left pointed triangles indicate the position of the three main wind jets identified in the January 2009 event. For display purposes, vectors are shown with a coarsened resolution (approximately 0.45°). (For interpretation of the references to color in this figure legend, the reader is referred to the web version of this article.)

which the winds are northward over the entire northern Red Sea. For example, Fig. 19a and b shows two examples of this large-scale northward winds, one in December 2003 that persist for 4 days in the 3-day moving average dataset and other in March 2004 with duration of 3 days. In the large-scale northward event of December 2003, the speeds can be as large as 8–9 m/s. In both cases, the RSCZ pattern is absent because the winds over the entire Red Sea blow northward (not shown).

In addition, the highest standard deviation in PC-1 occurs in winter (Fig. 18a, shading) and there is a seasonal modulation of the intraseasonal variability (not shown). A detailed investigation of this subject, however, is left for future work because the focus here is on the cross-axis winds.

The second EOF mode is characterized by cross-axis winds (Fig. 17b) and a strong seasonal cycle (Fig. 18b). This cross-axis wind mode emerges naturally from the EOF decomposition. This mode explains 10.7% of the wind variance and the cross-axis winds blow over

the entire northern Red Sea, which resembles the large-scale westward event composite of Fig. 16a. Westward winds, from Saudi Arabia to Africa, occur between October–April (winter monsoon) when the PC is positive (Fig. 18b). This EOF mode also suggests the existence of eastward winds over the entire northern Red Sea when the PC is negative, which generally occur in summer. Examining the QuikSCAT wind fields we find several examples of large-scale eastward winds, even in winter. For example, Fig. 19c shows a large-scale eastward event with wind speeds larger than 7 m/s in February 2007. This large-scale eastward event persisted for 5 days in the 3-day moving average dataset, with the RSCZ being absent in this period (not shown).

In the spatial pattern of the second EOF, the largest weights are found between 22° N–24° N, with a peak around 22.5° N (Fig. 20). According to the ETOPO2 data, the widest mountain gap along the Saudi Arabian coast (lowest average height) is found between 22° N–24° N (Fig. 3b). Interestingly, the latitudinal distribution of the second EOF cross-axis component in the eastern basin has minima

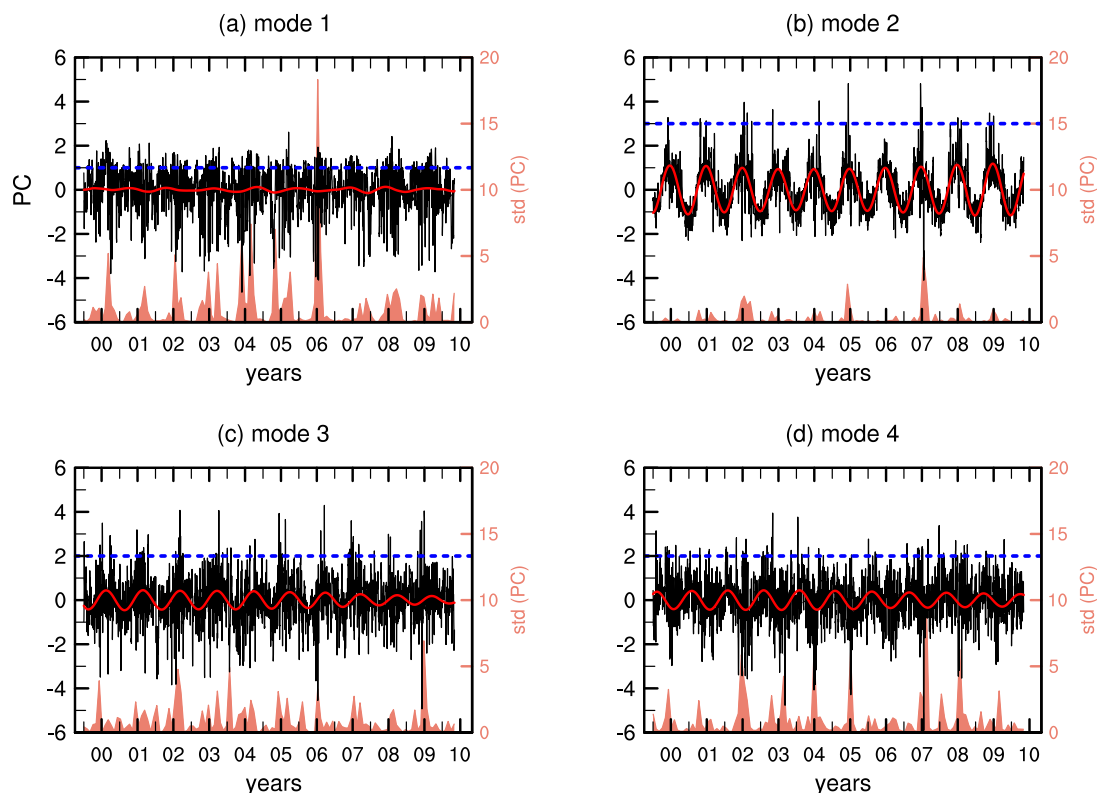


Fig. 18. The PC time series for each EOF mode shown in Fig. 17 (black curves). Red curves are the filtered annual bands and the salmon shadings are the monthly standard deviation of the respective PCs (right vertical-axis). Dashed blue lines indicate the PC values adopted to reconstruct the wind fields used to derive the wind stress curls shown in Fig. 17. (For interpretation of the references to color in this figure legend, the reader is referred to the web version of this article.)

Table 3

Explained variance (%) by period bands for the first four Principal Components (PC). *intra* refers to intraseasonal variability ($T \leq 150$ days), *semi* to semi-annual ($150 < T \leq 210$ days), *qa* between semi-annual and annual ($210 < T \leq 340$ days), *annual* ($340 < T \leq 438$ days) and *inter* to interannual variability ($T \geq 1.2$ years).

PC	intra	semi	qa	annual	inter
1	93.1	2.3	1.9	1.1	1.4
2	41.8	2.6	1.4	53.7	0.3
3	88.6	2.0	1.0	6.6	1.6
4	88.2	1.9	1.0	7.2	1.5

(westward maxima) that correspond with mountain gaps (compare Fig. 20 to Fig. 3b). Contrary to the other EOF modes, the annual band explains more than half of the PC variance (Table 3). The main spectral peak in the intraseasonal band is at 36 days, but there are secondary peaks occurring at about 20 days and 78 days.

The spatial pattern of the third EOF mode (8.8% of variance) is more complex (Fig. 17c). The winds north of about 23° N blow in opposite direction to the winds south of this latitude, forming a convergence/divergence zone between 22° N–24° N depending on the PC signal (negative/positive). This mode may be capturing the migration of the Red Sea RSCZ into our study area that sometimes is located as far north as 22° N (Ralston et al., 2013). According to QuikSCAT, around 5% of the winter days the RSCZ is located between 22° N–24° N (Fig. 10). Besides the RSCZ, QuikSCAT fields sometimes also exhibit a divergence zone in this area (e.g., Fig. 19d), which is consistent with the third EOF spatial pattern. This is the same region where several mountain gaps exist along the Saudi Arabian coast (Fig. 3a). It is possible that this mode might also be capturing some orographic effects on the surface winds. Similar to the leading EOF mode, the third PC is also dominated by intraseasonal variations with a main spectral peak at 35 days and a secondary peak at 68 days (Table 3).

The fourth mode has an interesting spatial pattern, but it only accounts for 3.2% of the variance. This pattern is characterized by cross-axis winds blowing in opposite directions north/south of 22° N–24° N. The winds are westward north of 24° N and eastward south of 22° N, which form a kind of counter-clockwise (cyclonic) gyre centered at 23.5° N (Fig. 17d). During winter (January–April), the PC values tend to be more negative, which reverts the gyre direction to anti-cyclonic. Most of the temporal variance is explained by intraseasonal variations with a main spectral peak at 79 days and a secondary peak at 34 days (Table 3).

To verify the robustness of the cross-axis mode, we performed three complementary EOF decompositions. In the first case, we removed the annual cycle prior to the EOF analysis. In this new decomposition, the cross-axis winds appear as the third EOF mode, explaining 5.8% of the total variance. The respective PC has two spectral peaks one at about 20 days (main peak) and other around 35 days (secondary), which are similar to the peaks described for the intra-seasonal band of the cross-axis mode in our first EOF decomposition. The first mode of the new decomposition (59.1% of the variance) is similar to Fig. 17a while the second mode (9.1%) is similar to Fig. 17c. The fourth mode explains 3.2% of the variance and is similar to the fourth mode of the first EOF analysis. In the second case, only wind fields during the winter monsoon (October–April) are considered. Again, the cross-axis winds appear as the third EOF mode but accounting for 7.1% of the variance. In this latter decomposition, the first mode explaining 60.9% of the variance is also similar to Fig. 17a. The second mode accounts for 8.7% of the variance and its pattern is similar to Fig. 17c. For the third case, the wind fields of the entire Red Sea are considered, and not only the northern Red Sea as previously. The cross-axis winds show up in the third and fourth modes explaining 6.6% of the variance (third mode with 4.6%). The first two modes show along-axis winds, one more important in the southern (leading mode) and the other in the northern Red Sea. The cross-axis mode is thus a robust feature of the Red Sea

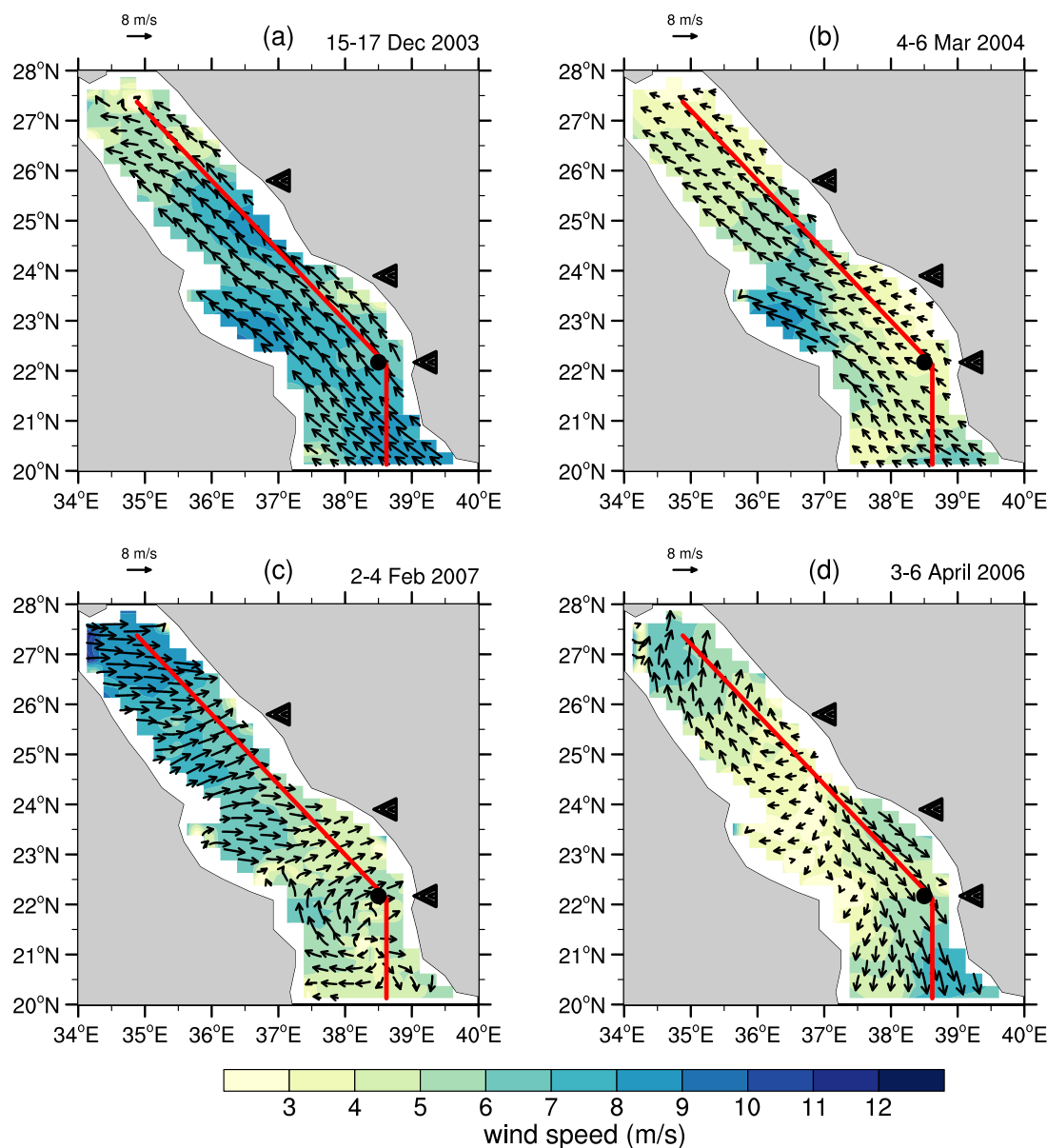


Fig. 19. QuikSCAT 3-days average wind fields over the northern Red Sea similar to: (a–b) the EOF leading mode for negative PCs; (c) the second EOF (also for negative PCs); (d) the third EOF for positive PCs. For display purposes, vectors are shown with a coarsened resolution (approximately 0.45°). The red line is the reference line and the black dot shows the WHOI/KAUST mooring position. Left pointed triangles indicate the position of the three main wind jets identified in the January 2009 event. (For interpretation of the references to color in this figure legend, the reader is referred to the web version of this article.)

wind variability.

The curl patterns derived from the four EOF spatial patterns shown in Fig. 17 are distinct. To compute the curl fields associated with each EOF mode, the wind components were reconstructed as usual in EOF analysis: $r_i(x,t) = PC_i(t)EOF_i(x)$ where r_i is the reconstruction for mode i , t is time, x is the grid point (lat,lon), $EOF_i(x)$ is the spatial pattern and $PC_i(t)$ is the time component of the EOF expansion (e.g., Kaihatu et al., 1998; Bjornsson and Venegas, 1997). To illustrate the differences in the curl spatial distribution associated with the four EOF patterns, Fig. 17 (colors) shows a set of examples which correspond to the times t when PC_i have the following values: 1 for the leading mode, 3 for the second mode and 2 for the third and fourth modes (Fig. 18, dashed blue lines). These PC_i values enable us to use a single color scale for the curl magnitude for the four maps. Because the reconstructed wind spatial pattern for each mode i is determined by the respective $EOF_i(x)$, its curl spatial structure will be similar for all $PC_i(t)$ values of same sign. The first mode would cause positive curl in the eastern side and negative in

the western, resembling the pattern observed for the winter climatological field (Fig. 16c). The cross-axis winds (second EOF) would impose alternating bands of positive/negative curl along the northern Red Sea main axis (Fig. 17b), which is similar to the large-scale westward event composite and snapshot shown in Fig. 16. On the other hand, the third and fourth modes would result in single-sign curl.

The EOF analyses described above point out that the winds over the northern Red Sea are more complex and variable than previously thought. Another way to investigate the wind constancy is through the directional wind steadiness. Fig. 21 shows the time series of the monthly steadiness parameter average over the northern Red Sea. The wind direction tends to be more steady in summer, when the steadiness parameter is close to 1, than in the winter monsoon (0.6–0.9), which is similar what we found in the mooring data. Besides the seasonal characteristics, the steadiness also shows strong interannual variability, in agreement with the previous analyses.

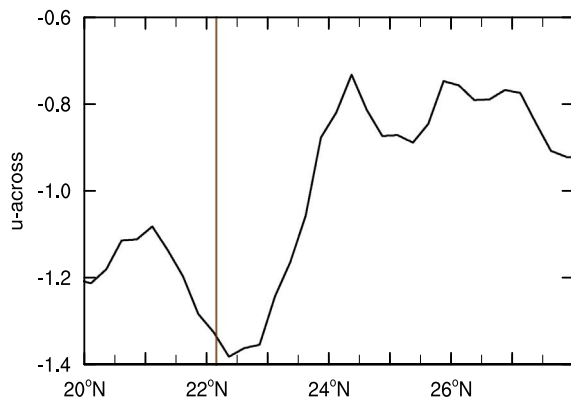


Fig. 20. Cross-axis component of the 2nd EOF mode along the northern Red Sea main axis. Negative values indicate westward direction. Vertical line marks the mooring position.

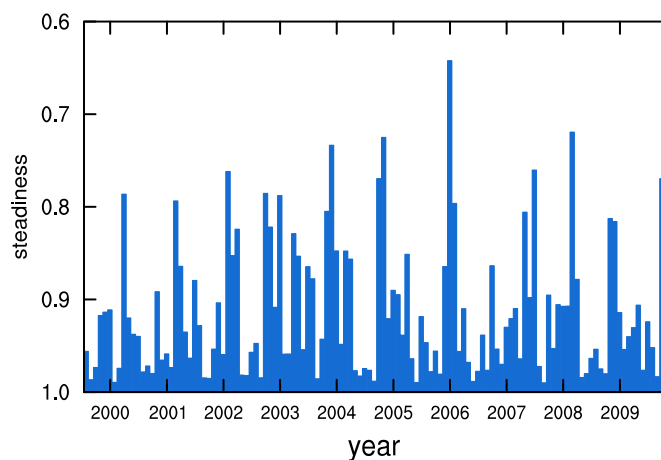


Fig. 21. Monthly directional wind steadiness from QuikSCAT averaged over the northern Red Sea (20° N–28° N). Steadiness close to one indicate a constancy in the direction of the monthly mean wind. Notice the winds over the northern Red Sea are less steady during the winter monsoon.

5. Summary & discussion

The 10-year long QuikSCAT record reveals a complex near-surface wind regime over the northern Red Sea. There are along- and across-axis wind patterns, with the southward-blowing winds dominating the temporal variability (56% of the wind variance). Cross-axis winds account for 11% of the variance, and 6.6% if the entire Red Sea is considered. The fact that the cross-axis wind pattern appears consistently as the second or the third EOF mode in four different EOF analyses indicates that these winds are not a rare pattern over the northern Red Sea. Direct examination of wind fields and the composite analysis confirm these findings. Surprisingly, QuikSCAT shows that occasionally the winds blow northward over the entire northern Red Sea even during the winter monsoon (October–April) and the RSCZ is not always present in this season. There are also some large-scale eastward events, from Africa to Saudi Arabia, which develop also in winter. These unexpected wind patterns can have duration of a couple of days and be relatively strong. The in situ observations at the WHOI/KAUST mooring corroborate these findings.

The above description is very different from how the winds in the northern Red Sea were previously described, i.e., relatively steady winds blowing southeastward all year round (e.g., Eshel et al., 1994; Patzert, 1974; Sofianos and Johns, 2003). It is also different from a seasonal description based on monthly mean climatologies where only the wind strength and the position of the RSCZ change during the

course of the year (e.g., Viswanadhapalli et al., 2017).

The fact that the near-surface winds are more complex than previously thought may have important implications for the understanding of the Red Sea dynamics, a subject of our on-going research.

When compared with in situ observations measured at the WHOI/KAUST mooring, QuikSCAT data are reproducing quite well the winds at that location. For wind speeds above 3 m/s, the correlation is 0.96 and the *rmsd* is 0.72 m/s, which is better than the global statistics (0.87 m/s) obtained by Ricciardulli and Wentz (2015) for the Ku-2011 GMF QuikSCAT products. For direction, correlation is 0.85 and the *rmsd* is 17.4°, which fall in the global expected range based on NCEP winds (9°–30° for speeds between 3–15 m/s) (Ricciardulli and Wentz, 2015). Previously, Ebuchi et al. (2002) evaluated QuikSCAT measurements using different GMFs (QSCAT-1 and Ku-2000) against in situ observations from the North Pacific and North Atlantic Oceans collected at the TAO/TRITON and PIRATA mooring arrays and NDBC (National Data Buoy Center) buoys. They found a global *rmsd* between 20.5° and 23.3° for speeds > 3 m/s.

In the northern Red Sea, Zhai and Bower (2013) found a *rmsd* of 29.9° and a correlation coefficient of 0.76 (direction) and 0.95 (speed) for winds stronger than 3 m/s. These statistics are based on the same in situ winds analysed here but using a previous version of RSS QuikSCAT product processed with the QSCAT-1 GMF (Wenz et al., 2001). The updated statistic indicate that the new version of the QuikSCAT data (Ku-2011 GMF) improved the agreement between satellite and in situ winds in the northern Red Sea, especially in relation to direction with correlation increasing from 0.76 to 0.85 and *rmsd* decreasing from 29.9° to 17.4°. The agreement between QuikSCAT and in situ winds is also robust for the wind components and other in situ time-averaging intervals (up to 4 h).

The decade-long QuikSCAT record confirms that westward winds, blowing from Saudi Arabia to Africa, are a typical wintertime phenomenon and occurs preferentially in December and January. This result is in agreement with the previous works by Bower and Farrar (2015), Jiang et al. (2009), Langodan et al. (2014) and Ralston et al. (2013) that described the westward winds arising in winter based on short-term WRF simulations and the WHOI/KAUST mooring data. During the overlapping period between QuikSCAT and the WHOI/KAUST mooring, there were three events (two in December 2008 and one in January 2009) in both datasets with similar strengths and durations.

Westward winds occur frequently in two regions, one between 21° N–24° N and other between 25° N–26° N, which correspond to the regions with lowest mean mountain height along the Saudi Arabian coast. Westward wind events can be composed by several wind jets and cover a large latitudinal range of the northern Red Sea. There are 18 large-scale westward events in the QuikSCAT record with duration between 3 and 8 days and strength varying from 3–4 to 9–10 m/s. The large-scale westward events are different from the wind pattern associated with the RSCZ, which is characterized by opposing along-axis winds that meet in the central Red Sea and bend westward towards the Tokar Gap direction. During the large-scale westward events, the winds over the entire northern Red Sea are westward while in the southern Red Sea they can be northward (more frequent) or southward.

A comparison between the QuikSCAT wind fields and the higher spatial resolution WRF simulations (Jiang et al., 2009; Kalenderski et al., 2013; Langodan et al., 2014; Ralston et al., 2013), and true-color MODIS images, indicate that standard QuikSCAT products do not resolve well the fine spatial structure of the westward wind events over the northern Red Sea. In the WRF simulations and the MODIS images, the westward events have a striking jet-like characteristic that is not so clear in the standard QuikSCAT wind fields due to its moderate spatial resolution (25 km). This resolution makes it difficult to resolve the narrow mountain-gap jets individually, since the jet separation can be 25–30 km or smaller. Moreover, the spatial resolution of QuikSCAT may not be appropriate to capture the wind jets in the extreme north,

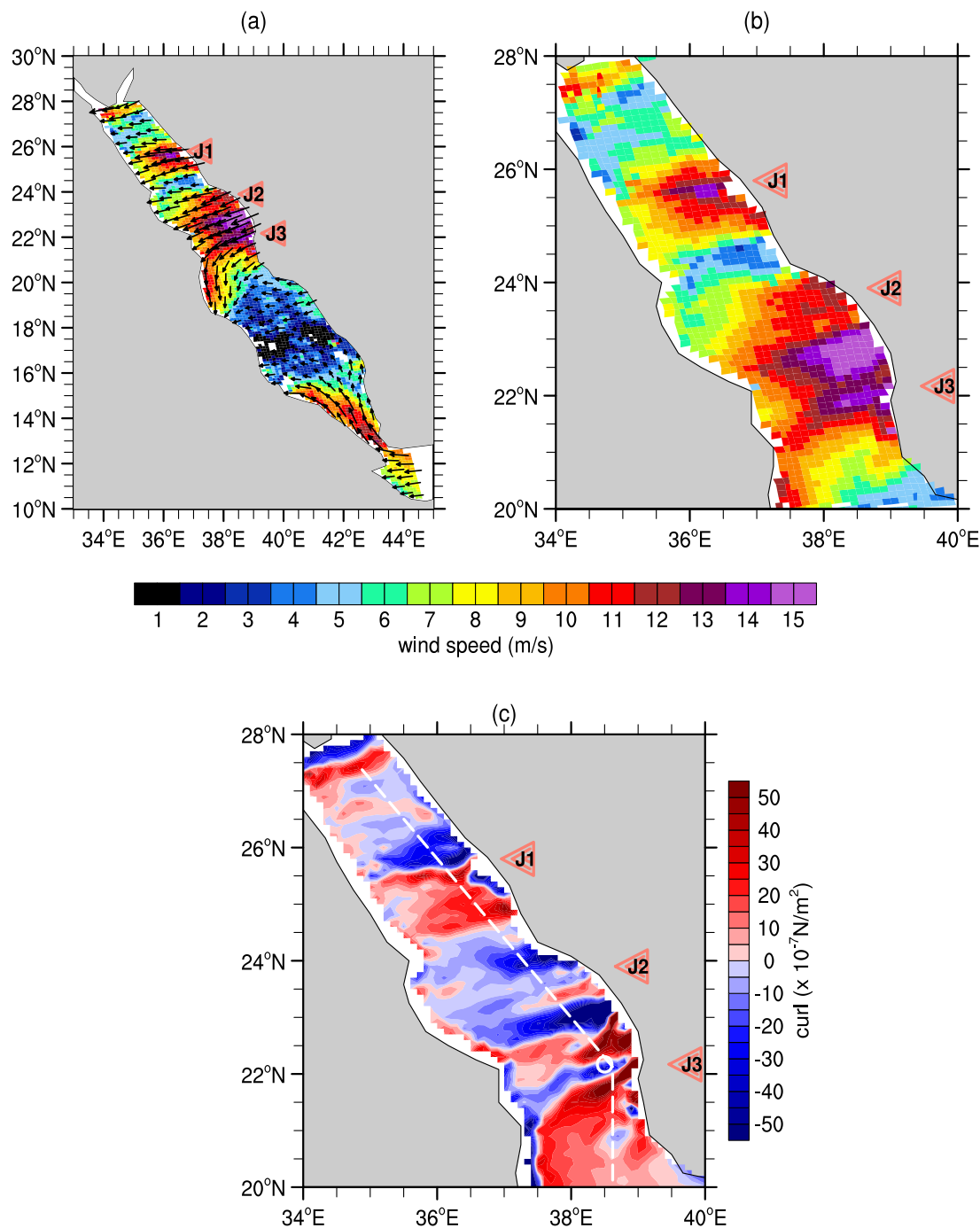


Fig. 22. Westward wind jets on 15 January 2009 0300 UTC as seen by the coastal QuikSCAT LCR Level 2B product v3.1 (similar to Fig. 5): (a) wind speed and direction for the entire Red Sea; (b) wind speed for the northern Red Sea; (c) wind stress curl. White line is the reference line and ring shows the WHOI/KAUST mooring position. Left pointed triangles indicate the position of the three main wind jets identified in the WRF simulation (J1, J2 and J3). For display purposes, vectors in (a) are shown with a coarsened resolution (approximately 0.57°).

where the mountain gaps are narrower. Hence, QuikSCAT probably overestimates the area of the northern Red Sea over which the winds blow westward and underestimates the jet effects on the wind stress curl. But, as we have shown, QuikSCAT wind stress curl fields are able to capture, although not completely, the jet effects.

We expect the QuikSCAT limitations described above will decrease in the near future with the new QuikSCAT coastal wind products that are being developed (Stiles et al., 2017). To avoid land contamination, the QuikSCAT standard processing omits measurements within 20 km of the coast but the new algorithms used for the coastal products such as the Land Contamination Ratio (LCR) allow data retrieval in the coastal band. Coastal QuikSCAT products reach higher spatial resolution

(12.5 km) through special processing. Using the LCR algorithm, JPL (NASA's Jet Propulsion Laboratory) has already produced global Level 2B (swath) wind fields for the QuikSCAT mission period but a better solution is being implemented (LCRES - Land Contamination Ratio Expected Sigma-0) (Stiles et al., 2017). As an example of the coastal QuikSCAT improvements in retrieving the westward mountain-gap wind jets, Fig. 22 shows the morning pass on 15 January 2009 processed with LCR: The winds are defined closer to the coastline and the coverage is better (much less missing data). The higher spatial resolution allows the coastal QuikSCAT to retrieve the wind jets in the extreme north and start to resolve some wind jets individually. The jet effects on the curl become much clearer (Fig. 22c). These new coastal

scatterometer data will allow important improvements in our understanding of the wind forcing for the Red Sea circulation and the wave state in the region (e.g. Langodan et al., 2014; Ralston et al., 2013).

We did not find a clear periodicity associated with the occurrence of westward events. Jiang et al. (2009) describe westward winds as occurring every 10–20 days in winter, but only based on a short-term WRF simulation (December 2008–January 2009). QuikSCAT also shows events occurring every 10–20 days in the same period. However, in the larger 10-year record, the westward winds appear as intermittent events with a strong interannual variability, although the cross-axis EOF mode has a primary or secondary spectral peak at about 20 days depending on the data input for the EOF. What causes winds to blow westward over the northern Red Sea in winter is still uncertain. Jiang et al. (2009) hypothesize that the westward wind jets may be due to local intensification of the Saudi Arabian High or the intrusion of cold air flowing from the Siberian High, a subject that is being investigated.

It is possible that climate modes may explain the observed inter-annual variability of westward events, especially the large-scale ones. Abualnaja et al. (2015) suggest that in winter the most important modes impacting the northern Red Sea are related to the North Atlantic Oscillation (NAO), the east Atlantic-west Russia teleconnection pattern and the interannual variability of the Indian monsoon regime. Relating the Red Sea large-scale westward wind events to climate modes is a topic for future study.

Bower and Farrar (2015) show that the mountain-gap westward winds strongly increase the heat loss and evaporation over the northern Red Sea. They found heat losses as large as -911 W/m^2 and evaporation rates far larger than 3 m/yr between 2008 and 2010 in the WHOI/KAUST mooring air-fluxes time series. QuikSCAT revealed westward winds are a relatively common wind pattern in winter. We can imagine that they may impact the ocean dynamics because evaporation is the main driver of the basin-scale Red Sea vertical overturning circulation (Bower and Farrar, 2015; Sofianos et al., 2015) and may influence the moisture transport over the adjacent continents (Zolina et al., 2017), but these impacts are not yet known and need to be investigated.

Besides potentially impacting the ocean through surface heat flux changes, the westward wind events impose a sequence of positive and negative wind stress curl along the main axis. This banded pattern contrasts with the normal along-axis winter condition, where the curl field is characterized by positive curl on the eastern side and negative curl on the western side. Similar to the effects of the Tehuantepec, Papagayo and Panama mountain-gap wind jets off the tropical eastern Pacific coast (McCreary et al., 1989; Chelton et al., 2000; Kessler, 2006) and the Tokar Gap wind jet (Zhai and Bower, 2013; Farley Nicholls et al., 2015) in the central Red Sea, the positive/negative curl pattern is expected to produce domes and bowls in the thermocline along the main axis, through upwelling/downwelling, and corresponding lows and highs in the sea surface height. Based on the McCreary et al. (1989) and Zhai and Bower (2013) models, we can speculate that the positive/negative curl pattern imposed by the westward wind events may be an important process leading to eddy formation in the northern Red Sea. There is some evidence to indicate this hypothesis may be true. Numerical simulations by Clifford et al. (1997) show that the Red Sea circulation is much more eddy-like when the winds are cross-axis. Bower and Farrar (2015) showed that during winter there is a banded structure of negative and positive relative vorticity in surface currents along the main Red Sea axis, but they did not associate this pattern with the occurrence of westward winds. Contrary to the previously cited works, Zhan et al. (2016) found that the eddy kinetic energy generated by winds is limited to the southern Red Sea and generally not important, but the wind fields used to force their model do not resolve mountain-gap wind jets. Hence, the way wind curl changes and heat fluxes associated with westward winds impact the ocean is still not well known and needs further study.

Acknowledgments

We wish to acknowledge the use of the Ferret program (NOAA/PMEL) and NCL for analysis and graphics in this paper. We thank Houshuo Jiang for sharing the WRF model outputs and Bryan Stiles for helping with the QuikSCAT coastal data. VVM also acknowledges Marcio Vianna for fruitful discussion about wind jets and their potential effects. QuikSCAT (or SeaWinds) data are produced by Remote Sensing Systems and sponsored by the NASA Ocean Vector Winds Science Team. Data are available at www.remss.com. WHOI/KAUST mooring data collected during the WHOI-KAUST collaboration was made possible by Award Nos. USA00001, USA00002, and KSA00011 to WHOI by KAUST in the Kingdom of Saudi Arabia. The data are available from the authors upon request. This work was supported by NSF grant OCE-1435665 and NASA grant NNX14AM71G.

References

- Abualnaja, Y., Papadopoulos, V.P., Josey, S.A., Hoteit, I., Kontoyiannis, H., Raitos, D.E., 2015. Impacts of climate modes on air-sea heat exchange in the Red Sea. *J. Climate* 28, 2665–2681.
- Beal, L.M., Field, A., Gordon, A.L., 2000. Spreading of Red Sea, overflow waters in the Indian Ocean. *J. Geophys. Res.* 105, 8549–8564.
- Berens, P., 2009. Circstat: a MATLAB toolbox for circular statistics. *J. Stat. Softw.* 31, 1–21.
- Bjornsson, H., Venegas, S.A., 1997. A Manual for EOF and SVD Analyses of Climate Data. Tech. Rep., McGill University CCGCR Report No. 97-1. Montreal, Quebec, pp. 52.
- Bourassa, M.A., Legler, D.M., O'Brien, J.J., Smith, S.R., 2003. SeaWinds validation with research vessels. *J. Geophys. Res.* 108 (C2), 3019.
- Bower, A.S., Farrar, J.T., 2015. Air-sea interaction and horizontal circulation in the Red Sea. In: Rasul, N.M.A., Stewart, I.C.F. (Eds.), *The Red Sea*. Springer Berlin Heidelberg, pp. 329–342.
- Brennan, M.J., Cobb, H.D.I., Knabb, R.D., 2010. Observations of Gulf of Tehuantepec, gap wind events from QuikSCAT: an updated event climatology and operational model evaluation. *Wea. Forecasting* 25, 646–658.
- Brodeau, L., Barnier, B., Gulev, S., Woods, C., 2017. Climatologically significant effects of some approximations in the bulk parameterizations of turbulent air-sea fluxes. *J. Phys. Oceanogr.* 47, 5–28.
- Chelton, D.B., Freilich, M.H., Esbensen, S.K., 2000. Satellite observations of the wind jets off the Pacific coast of Central America. Part I: case studies and statistical characteristics. *Mon. Wea. Rev.* 128, 1993–2018.
- Chelton, D.B., Schlax, M.G., Freilich, M.H., Milliff, R.F., 2004. Satellite measurements reveal persistent small-scale features in ocean winds. *Science* 303, 978–983.
- Chelton, D., Freilich, M., Sienkiewicz, J., Von Ahn, J., 2006. On the use of quikSCAT scatterometer measurements of surface winds for marine weather prediction. *Mon. Wea. Rev.* 134, 2055–2071.
- Churchill, J.H., Lentz, S.J., Farrar, J., Abualnaja, Y., 2014. Properties of Red Sea coastal currents. *Cont. Shelf Res.* 78, 51–61.
- Clifford, M., Horton, C., Schmitz, J., Kantha, L.H., 1997. An oceanographic nowcast/forecast system for the Red Sea. *J. Geophys. Res.* 102 (C11), 25101–25122.
- Cornillon, P., Park, K.A., 2001. Warm core ring velocities inferred from NSCAT. *Geophys. Res. Lett.* 28, 575–578.
- Davis, S.R., Pratt, L.J., Jiang, H., 2015. The Tokar gap jet: regional circulation, diurnal variability, and moisture transport based on numerical simulations. *J. Climate* 28, 5885–5907.
- Dorman, C.E., Carniel, S., Cavaleri, L., Sclavo, M., Chiggiato, J., Doyle, J., Haack, T., Pullen, J., Grbec, B., Vilibić, I., Janeković, I., Lee, C., Malačić, V., Orlić, M., Paschini, E., Russo, A., Signell, R.P., 2006. February 2003 marine atmospheric conditions and the bora over the northern Adriatic. *J. Geophys. Res.* 111, C03S03.
- Ebuchi, N., Graber, H., Caruso, M., 2002. Evaluation of wind vectors observed by quikSCAT/seawinds using ocean buoy data. *J. Atmos. Oceanic Tech.* 19, 2049–2062.
- Emery, W.J., Thomson, R.E., 2001. *Data Analysis Methods in Physical Oceanography*. Elsevier, New York.
- Eshel, G., Cane, M.A., Blumenthal, M.B., 1994. Modes of subsurface, intermediate, and deep water renewal in the Red Sea. *J. Geophys. Res.* 99, 15941–15952.
- Fairall, C.W., Bradley, E.F., Hare, J.E., Grachev, A.A., Edson, J.B., 2003. Bulk parameterization of air-sea fluxes: updates and verification for the COARE algorithms. *J. Climate* 16, 571–591.
- Farley Nicholls, J., Toumi, R., Stenchikov, G., 2015. Effects of unsteady mountain-gap winds on eddies in the Red Sea. *Atmosph. Sci. Lett.* 16, 279–284.
- Farrar, J.T., Lentz, S.J., Churchill, J.H., Bouchard, P.R., Smith, J.C., Kemp, J.N., Lord, J., Allsup, G.P., Hosom, D.S., 2009. King Abdullah University of Science and Technology (KAUST) Mooring Deployment Cruise and Fieldwork Reports. Tech. Rep. Woods Hole Oceanographic Institution.
- Fisher, N.I., 1996. *Statistical Analysis of Circular Data*. Cambridge University Press, Cambridge, UK.
- Fu, L.L., Morrow, R., 2013. Chapter 4 - remote sensing of the global ocean circulation. In: Siedler, G., Stephen, M., Griffes, J., Gould John, A.C. (Eds.), *International Geophysics*. vol. 103. Academic Press, pp. 83–111.
- Ghil, M., Allen, M.R., Dettinger, M.D., Ide, K., Kondrashov, D., Mann, M.E., Robertson,

- A.W., Sounders, A., Tian, Y., Varadi, F., Yiou, P., 2002. Advanced spectral methods for climatic time series. *Rev. Geophys.* 40 (1) 3.1–3.41.
- Gille, S.T., Llewellyn Smith, S.G., Lee, S.M., 2003. Measuring the sea breeze from quikSCAT scatterometry. *Geophys. Res. Lett.* 30, 1114.
- Han, W., McCreary, J., 2001. Modeling salinity distributions in the Indian Ocean. *J. Geophys. Res.* 206, 859–877.
- Hoffman, R.N., Leidner, S.M.L., 2005. An introduction to the near-real time quikSCAT data. *Wea. Forecasting* 20, 476–493.
- Holbach, H., Bourassa, M., 2014. The effects of gap-wind-induced vorticity, the monsoon trough, and the ITCZ on East Pacific tropical cyclogenesis. *Mon. Wea. Rev.* 142, 1312–1325.
- Jiang, H., Farrar, J.T., Beardsley, R.C., Chen, R., Chen, C., 2009. Zonal surface wind jets across the Red Sea due to mountain gap forcing along both sides of the Red Sea. *Geophys. Res. Lett.* 36, L19605.
- Johns, W.E., Jacobs, G.A., Kindle, J.C., Murray, S.P., Carron, M., 1999. Arabian Marginal Seas and Gulfs: Report of a Workshop Held at Stennis Space Center, Miss. 11–13 May, 1999. Tech. rep. University of Miami RSMAS Technical Report 2000-01.
- Kaihatu, J.M., Handler, R.A., Marmorino, G.O., Shay, L.K., 1998. Empirical orthogonal function analysis of ocean surface currents using complex and real-vector methods. *J. Atmos. Oceanic Tech.* 15, 927–941.
- Kalenderski, S., Stenichikov, G., Zhao, C., 2013. Modeling a typical winter-time dust event over the Arabian peninsula and the Red Sea. *Atmos. Chem. Phys.* 13, 1999–2014.
- Kelly, K.A., Dickinson, S., McPhaden, M.J., Johnson, G.C., 2001. Ocean currents evident in satellite wind data. *Geophys. Res. Lett.* 28, 2469–2472.
- Kessler, W.S., 2006. The circulation of the Eastern Tropical Pacific: a review. *Progr. Oceanogr.* 69, 181–217.
- Langodan, S., Cavaleri, L., Viswanadhappalli, Y., Hoteit, I., 2014. The Red Sea: a natural laboratory for wind and wave modeling. *J. Phys. Oceanogr.* 44, 3139–3159.
- Langodan, S., Cavaleri, L., Viswanadhappalli, Y., Hoteit, I., 2015. Wind-wave source functions in opposing seas. *J. Geophys. Res.* 120, 6751–6768.
- Langodan, S., Cavaleri, L., Vishwanadhappalli, Y., Pomaro, A., Bertotti, L., Hoteit, I., 2017. The climatology of the Red Sea - part 1: the winds. *Int. J. Climatol.*
- Large, W.G., McWilliams, J.C., Doney, S.C., 1994. Oceanic vertical mixing: a review and a model with a nonlocal boundary layer parameterization. *Rev. Geophys.* 32, 363–403.
- Lee, C.M., Askari, F., Book, J., Carniel, S., Cushman-Roisin, B., Dorman, C., Doyle, J., Flament, P., Harris, C.K., Jones, B.H., Kuzmic, M., Martin, P., Ogston, A., Orlic, M., Perkins, H., Poulain, P.-M., Pullen, J., Russo, A., Sherwood, C., Signell, R.P., Thaler, D., 2005. Northern Adriatic response to a wintertime bora wind events. *Eos Trans. AGU*, 86, 157–165.
- Ludwig, F.L., Horel, J., Whiteman, C.D., 2004. Using EOF analysis to identify important surface wind patterns in mountain valleys. *J. Appl. Meteor.* 43, 969–983.
- Marshall, J., Ferrari, R., Forget, G., Maze, G., Andersson, A., Bates, N., Dewar, W., Doney, S., Fratantoni, D., Joyce, T., Straneo, F., Toole, J., Weller, R., Edson, J., Gregg, M., Kelly, K., Lozier, S., Palter, J., Lumpkin, R., Samelson, R., Skillingstad, E., Silverthorne, K., Talley, L., Thomas, L., 2009. The Climode field campaign: Observing the cycle of convection and restratification over the Gulf Stream. *Bull. Amer. Meteor. Soc.* 90, 1337–1350.
- McCreary, J.P., Lee, H.S., Enfield, D.B., 1989. The response of the coastal ocean to strong offshore winds: With application to circulations in the gulfs of Tehuantepec and Papagayo. *J. Mar. Res.* 47, 81–109.
- Menezes, V.V., Vianna, M.L., Phillips, H.E., 2014. Aquarius sea surface salinity in the South Indian Ocean: Revealing annual-period planetary waves. *J. Geophys. Res.* 119, 3883–3908.
- Menezes, V.V., Phillips, H.E., Vianna, M.L., Bindoff, N.L., 2016. Interannual variability of the South Indian Countercurrent. *J. Geophys. Res.* 121, 3465–3487.
- NCL, 2017. The NCAR Command Language (Version 6.1.2) (Version 6.4.0) [Software]. Boulder, Colorado: UCAR/NCAR/CISL/TDD. <http://dx.doi.org/10.5065/D6WD3XH5>.
- NGDC, 2006. National Geophysical Data Center. 2-minute Gridded Global Relief Data (ETOPO2) v2. National Geophysical Data Center, NOAA. <http://dx.doi.org/10.7289/V5J1012Q>.
- O'Neill, L., Chelton, D., Esbensen, S., Wentz, F., 2005. High-resolution satellite measurements of the atmospheric boundary layer response to SST variations along the Agulhas Return Current. *J. Climate* 18, 2706–2723.
- O'Neill, L., Chelton, D., Esbensen, S., 2010. The effects of SST-induced surface wind speed and direction gradients on midlatitude surface vorticity and divergence. *J. Climate* 23, 255–281.
- Papadopoulos, V.P., Abualnaja, Y., Josey, S.A., Bower, A., Raitsos, D.E., Kontoyiannis, H., Hoteit, I., 2013. Atmospheric forcing of the winter air-sea heat fluxes over the northern Red Sea. *J. Climate* 593, 1685–1701.
- Patzert, W.C., 1974. Wind-induced reversal in Red Sea circulations. *Deep-Sea Res.* 21, 109–121.
- Pedgley, D.E., 1966a. The Red Sea Convergence Zone. Part I - the horizontal pattern of winds. *Weather* 21, 350–358.
- Pedgley, D.E., 1966b. The Red Sea Convergence Zone. Part II - vertical structure. *Weather* 21, 394–406.
- Poulain, P.M.V.H.K., Cushman-Roisin, B., 2001. Northern Adriatic Sea. In: Cushman-Roisin, B., Gacic, M., Poulain, P.M., Artegiani, A. (Eds.), *Physical Oceanography of the Adriatic Sea*. Springer, Dordrecht, pp. 143–165.
- Ralston, D.K., Jiang, H., Farrar, J.T., 2013. Waves in the Red Sea: response to monsoonal and mountain gap winds. *Cont. Shelf Res.* 65, 1–13.
- Ricciardulli, L., Wentz, F.J., 2015. A scatterometer geophysical model function for climate-quality winds: QuikSCAT Ku-2011. *J. Atmos. Oceanic Tech.* 32, 1829–1846.
- Ricciardulli, L., Wentz, F.J., Smith, D.K., 2011. Remote Sensing Systems QuikSCAT Ku-2011 3-Day Ocean Vector Winds on 0.25 Deg Grid, Version 4. Remote Sensing Systems. Santa Rosa, CA. Available online at <http://www.remss.com/missions/qscat>. [Accessed 20 Jan 2016]. Tech. rep., Remote Sensing Systems.
- Risien, C., Chelton, D.B., 2008. A global climatology of surface wind and wind stress fields from eight years of quikSCAT scatterometer data. *J. Phys. Oceanogr.* 38, 2379–2413.
- Singer, I.A., 1967. Steadiness of the winds. *J. Appl. Meteor.* 6, 1033–1038.
- Smith, W.H.F., Sandwell, D.T., 1997. Global seafloor topography from satellite altimetry and ship depth soundings. *Science* 277, 1956–1962.
- Sofianos, S.S., Johns, W.E., 2003. An oceanic general circulation model (OGCM) investigation of the Red Sea circulation: 2. Three-dimensional circulation in the Red Sea. *J. Geophys. Res.* 108, 3066.
- Sofianos, S., Johns, W.E., 2015. Water mass formation, overturning circulation, and the exchange of the Red Sea with the adjacent basins. In: Rasul, N.M.A., Stewart, I.C.F. (Eds.), *The Red Sea*. Springer Berlin Heidelberg, pp. 343–354.
- Steedman, R.A., Ashour, Y., 1976. Sea breezes over north-west Arabia. *Tellus* 28A, 299–306.
- Stiles, B., Fore, A.G., Strub, P.T., James, C., 2017. QuikSCAT coastal wind products. In: NASA OVWST and International OVWST Meeting 2017.
- Stoffelen, A., 1988. Toward the true near-surface wind speed: error modeling and calibration using triple collocation. *J. Geophys. Res.* 103, 7755–7766.
- Tragou, E., Garrett, C., Outerbridge, R., Gilman, C., 1999. The heat and freshwater budgets of the Red Sea. *J. Phys. Oceanogr.* 29, 2504–2522.
- Vianna, M.L., Menezes, V.V., 2006. Singular spectrum analysis of nonstationary tidal currents applied to ADCP data from the northeast Brazilian shelf. *J. Atmos. Oceanic Tech.* 23, 138–151.
- Vianna, M.L., Menezes, V.V., 2013. Bidecadal sea level modes in the North and South Atlantic Oceans. *Geophys. Res. Lett.* 40, 5926–5931.
- Viswanadhappalli, Y., Dasari, H.P., Langodan, S., Challa, V.S., Hoteit, I., 2017. Climatic features of the Red Sea from a regional assimilative models. *Int. J. Climatol.* 37, 25632581.
- Weissman, D.E., Bourassa, M.A., Tongue, J., 2002. Effects of rain rate and wind magnitude on SeaWinds scatterometer wind speed errors. *J. Atmos. Oceanic Tech.* 19, 738–746.
- Wentz, F.J., Smith, D.K., Mears, C.A., Gentemann, C.L., 2001. Advanced algorithms for QuikSCAT and SeaWinds/AMSR. In: IGARSS 2001 Sydney Australia. Scanning the Present and Resolving the Future. Proceedings. IEEE 2001 International Geoscience and Remote Sensing Symposium. Vol. 3. pp. 1079–1081.
- Zar, J.H., 2010. *Biostatistical Analysis*, 5th ed. Pearson Prentice Hall.
- Zhai, P., Bower, A.S., 2013. The response of the Red Sea to a strong wind jet near the Tokar Gap in summer. *J. Geophys. Res.* 118, 422–434.
- Zhan, P., Subramanian, A.C., Yao, F., Kartadikaria, A.R., Guo, D., Hoteit, I., 2016. The eddy kinetic energy budget in the Red Sea. *J. Geophys. Res.* 121, 4732–4747.
- Zolina, O., Dufour, A., Gulev, S., Stenichikov, G., 2017. Regional hydrological cycle over the Red Sea in ERA-interim. *J. Hydrometeorol.* 18, 65–83.